Ⓔ

FIRST 3D RECONSTRUCTIONS OF CORONAL LOOPS WITH THE *STEREO A+B* SPACECRAFT. II. ELECTRON DENSITY AND TEMPERATURE MEASUREMENTS

MARKUS J. ASCHWANDEN, NARIAKI V. NITTA, JEAN-PIERRE WUELSER, AND JAMES R. LEMEN
Lockheed Martin Advanced Technology Center, Solar and Astrophysics Laboratory, Organization ADBS,
Building 252, 3251 Hanover Street, Palo Alto, CA 94304; aschwanden@lmsal.com

ABSTRACT

Using the stereoscopically derived three-dimensional (3D) geometry of 30 loops observed with *STEREO* EUVI (described in Paper I) we determine here the electron density profiles $n_e(s)$ and electron temperature profiles $T_e(s)$ from a triple-filter analysis of the stereoscopic images taken in the wavelengths of $\lambda = 171$, 195, and 284 Å. The statistical results of our analysis of seven complete loops are: observed loop widths $w_{\rm obs} = 2.6 \pm 0.1$ Mm, corresponding to effective loop widths of $w = 1.1 \pm 0.3$ Mm if corrected for the instrumental point-spread function; loop flux ratios $f_{\rm loop}/f_{\rm total} = 0.11 \pm 0.04$; mean loop (DEM peak) temperatures $T_p = 1.1 \pm 0.2$ MK; DEM temperature Gaussian widths $\sigma_{\rm DEM} = 0.35 \pm 0.04$ MK; temperature variations along loops $\sigma_T/T_p = 0.24 \pm 0.05$; (resolution-corrected) loop base densities $n_e = (2.2 \pm 0.5) \times 10^9$ cm^{-3}; loop lengths of $L = 130 \pm 67$ Mm; and all quantities are found to agree between *STEREO A* and *B* within a few percent. The temperature profiles $T(s)$ along loops are found to be nearly constant, within the uncertainties of the background subtraction. The density profiles $n_e(s)$ are consistent with the gravitational stratification of hydrostatic loops, $n_e(h) = n_{\rm base} \exp(-h/\lambda_T)$, defined by the temperature scale heights λ_T and stereoscopically measured from the height profiles $h(s)$. The stereoscopic 3D reconstruction allows us for the first time to accurately measure the loop length L and to test loop scaling laws. We find that the observations are not consistent with equilibrium solutions, but rather display the typical overpressures of loops that have been previously heated to higher temperatures and cool down in a nonequilibrium state, similar to earlier EIT and *TRACE* measurements.

Subject headings: Sun: corona — Sun: UV radiation

Online material: color figures

1. INTRODUCTION

Stereoscopic observations provide more rigorous and precise methods to measure physical parameters in coronal loops, such as the electron density or the electron temperature, which is the focus of this study. We face the challenging additional constraint of obtaining self-consistent solutions from the images of two independent spacecraft that have different stereoscopic viewing angles. Our task is (1) to identify corresponding loop features in two stereoscopic images and to measure the 3D coordinates of such an identical loop; and (2) to extract the cross-sectional flux profiles of this identical loop from two different backgrounds (seen from two different lines of sight), which entirely control the outcome of obtaining self-consistent loop widths, densities, temperatures, and loop-associated differential emission measure (DEM) distributions from the two spacecraft images. The task is particularly challenging because the loop-associated EUV fluxes typically amount only to ≲10% of the total flux along a given line of sight, and thus we are in the situation of inferring loop parameters from the small difference of two large quantities (total flux minus background flux). Therefore, the background has to be determined in each spacecraft with an accuracy of ≈1% in order to obtain ≈10% self-consistency between the densities, filter ratios, or DEMs of loop parameters between the two spacecraft. Methods to determine loop densities and temperatures with arbitrary background subtraction (or with no background subtraction at all), as they have been inappropriately applied in earlier publications, are unacceptable for the stereoscopic analysis attempted here. In this study we will test a number of various background subtraction methods, whose quality and appropriateness can now be rigorously tested by comparing the self-consistency of the solutions between the two stereoscopic spacecraft. Therefore,

the availability of stereoscopic data opens up a new double-check method to assess the accuracy of physical parameters determined in coronal loops.

The soft X-ray (SXR) and extreme ultraviolet (EUV) emission of the Sun in active regions harbors hot thermal plasma at temperatures in the range of ≈10^6–10^7 K. When we point high-resolution imagers (e.g., *SOHO* EIT, *TRACE*, *STEREO* EUVI, and *Hinode* EIS) to such active regions we can discern very fine loops or loop strands in the solar corona if we display the images with appropriate high-pass filters to enhance the smallest spatial scales. It has been recently found that loop strands with typical widths of $w \approx 1.4 \pm 0.3$ Mm have a near-isothermal cross section based on a triple-filter temperature analysis method (Aschwanden & Nightingale 2005; Aschwanden 2005), while virtually all loop structures with larger diameters have a broad temperature distribution (e.g., Schmelz et al. 2001; Schmelz & Martens 2006). Although there are some confusing comments in the literature about thermal and multithermal loops, there seems to be a clear dividing line that only the smallest observed loop strands with widths of $w \lesssim 1.5$ Mm are near-isothermal, which we refer to as *elementary loops*, while virtually all wider loops are multithermal, which we refer to as *composite loops* (Aschwanden 2005). Of course, only elementary loops can be used for 1D hydrodynamic modeling, because the assumption is made in 1D models that the flux tube has a homogeneous cross section (in temperature and density). On the other side, composite loops can only be modeled in terms of statistical models, such as the concepts of most nanoflare models (e.g., Klimchuk et al. 2008).

In a previous paper (Aschwanden et al. 2008, hereafter Paper I) we determined the 3D geometry of the 30 finest loops detected in an active region, which are candidates for elementary loop structures, a hypothesis that can only be tested with a suitable

TABLE 1
PARAMETERS OF SIX ANALYZED *STEREO* IMAGES ON 2007 MAY 9

Observing Time (UT)	Spacecraft *STEREO*	Wavelength (Å)	Exposure Time (s)	Sun Center (x-pixel)	Sun Center (y-pixel)	Solar Radius (arcsec)	Roll Angle (deg)
20:40:45.006	A	171	4.002	1020.63	926.70	998.962	7.196
20:41:29.966	B	171	4.002	1035.55	1051.08	913.579	13.086
20:41:20.022	A	195	4.002	1020.63	926.70	998.962	7.196
20:42:04.992	B	195	4.005	1035.55	1051.08	913.579	13.086
20:41:55.008	A	284	16.000	1020.63	926.70	998.962	7.196
20:42:39.965	B	284	16.004	1035.55	1051.08	913.579	13.086

temperature analysis. In this paper we concentrate on an accurate determination of the electron density and electron temperature of these 30 finest loop structures by stereoscopic methods. The rationale for this task is motivated in many ways. First, as mentioned above, the self-consistency between the solutions from both spacecraft reinforces a higher reliability and accuracy of the physical parameters of density n_e, temperature T_e, and loop width w. The additional reconstruction of the 3D geometry provides accurate loop heights and inclination angles of the loop plane, which is a prerequisite to determine the vertical density (or pressure) scale height that is needed in assessing the hydrodynamic momentum balance. The stereoscopically evaluated 3D geometry also yields an accurate measurement of the total loop length L (appearing only in 2D projection in single-spacecraft images), which permits us for the first time a rigorous test of loop scaling laws (e.g., the Rosner-Tucker-Vaiana [RTV] law). Moreover, we can then determine parameters of both equilibrium and nonequilibrium models more precisely, which provide crucial diagnostics on the heating function. Finally, the determination of the density and temperature structure of the finest detectable loops in an active region can then be used as a skeleton for a full 3D rendering of the plasma in an active region based on physical 3D models (e.g., Schrijver et al. 2004), to predict images for different instruments with different wavelengths and temperature filters (subject of future studies).

The plan of this paper is as follows: The data analysis method is described in § 2, the results are presented in § 3, a discussion of a few new aspects is given in § 4, and conclusions are summarized in § 5.

2. DATA ANALYSIS METHODS

2.1. *Observations and Data Set*

The data analysis in this study is an expansion of the first study (Paper I), where the 3D geometry of 30 active region loops was determined based on Extreme Ultra-Violet Imager (EUVI) images observed with the two *STEREO* spacecraft A (ahead) and B (behind) on 2007 May 9, around 20 : 40 UT, in the 171 Å wavelength. In this study we include additionally the stereoscopic images of the A and B spacecraft in the 195 and 284 Å wavelengths. This is a set of three image pairs, each of which was taken strictly simultaneously on the Sun in each wavelength (after correction for the light-travel time difference between the two spacecraft positions), while the observing program sequentially stepped through the three wavelengths. The 195 Å (and 284 Å) images were taken 35 s (and 70 s) after the 171 Å images. All images have a size of 2048×2048 and a pixel size of $1.5877'' \times 1.5900''$. The effective spatial resolution (or FWHM of the point-spread function) is approximately 2 EUVI pixels (Wuelser et al. 2004), which corresponds to $\approx 3.2''$ or 2300 km. A preliminary analysis of the lunar transit on 2007 February 25 for *STEREO B* yielded a point-spread function approaching a width of $3.5''$, i.e., 2.2 EUVI pixels (Lemen

et al. 2007). We list the observing times, wavelengths, exposure times, Sun center positions, solar radii, and spacecraft roll angles of the six analyzed images in Table 1. The spacecraft separation angle is $\alpha_{\rm sep} = 7.257°$ at this time, and the spacecraft plane (defined by the spacecraft positions A and B and the Sun center) is inclined by $\alpha_{AB} = 9.056°$ to the ecliptic plane.

We coalign the $A+B$ image pairs from the two spacecraft in each wavelength with the same procedure as described in Paper I and find subpixel accuracy for the stereoscopic image pairs (in each wavelength separately). In addition, the images in different wavelengths on the same spacecraft are assumed to be coaligned with subpixel accuracy because they are produced with the same optics and CCD, save for optical aberration errors and spacecraft jitter during the time interval of subsequent images (of different wavelengths on the same spacecraft). We show a synopsis of six subimages encompassing the northern half of the active region in Figure 1, where we display the EUV brightness on a logarithmic color scale, with one particular loop (No. 3 in Paper I) outlined in each image. The active region is located approximately $30°$ east of Sun center near the equator. Unfortunately, there were no observations of this active region by *TRACE* on the same day.

2.2. *EUVI Temperature Response Functions*

The EUVI response functions for the 171, 195, and 284 Å filters are shown in the temperature range of $T = 0.3–3.0$ MK for both the EUVI A and B spacecraft in Figure 2. For more detailed information see Wuelser et al. (2004). The response functions have been calculated from preflight calibration results using the line emissions from the CHIANTI software (Young et al. 2003), assuming coronal elemental abundances (Feldman 1992) and the ionization equilibrium of Mazotta et al. (1998). The response functions in Figure 2 are given in units of photons s^{-1} for an emission measure of EM $= n_e^2 V = 10^{44}$ cm^{-3} [which corresponds to a density of $n_e = 10^{10}$ cm^{-3} for a volume of $V = (10^8$ cm$)^3$]. For the conversion into observed data numbers (DN s^{-1}) we need two factors: (1) the conversion factor q_1 of incoming photons to electrons that are produced by the photoelectric effect in the silicon of the CCD, which is the energy of the incoming photon ($\varepsilon = 12.4$ keV/λ[Å], i.e., 72.5, 63.6, and 43.7 eV for the 171, 195, and 284 Å filters, respectively) divided by the silicon band gap energy of $\Delta\varepsilon = 3.65$ eV, so $q_1 = \varepsilon/\Delta\epsilon = 19.9, 17.4,$ and 12.0 for these filters; and (2) the gain factor q_2 of electrons to DN, which is $q_2 \approx 1/15$ according to preflight calibrations. Thus, the combined conversion factor $q = q_1 q_2$ from incoming photons to image data numbers (DN) is $q_{171} = 1.32$ for 171 Å, $q_{195} = 1.16$ for 195 Å, and $q_{284} = 0.80$ for 284 Å.

2.3. *Loop Background Subtraction Methods*

The derivation of the electron temperature profile $T_e(s)$ and electron density $n_e(s)$ along the loop coordinate s requires background-subtracted EUV fluxes in each wavelength. The most
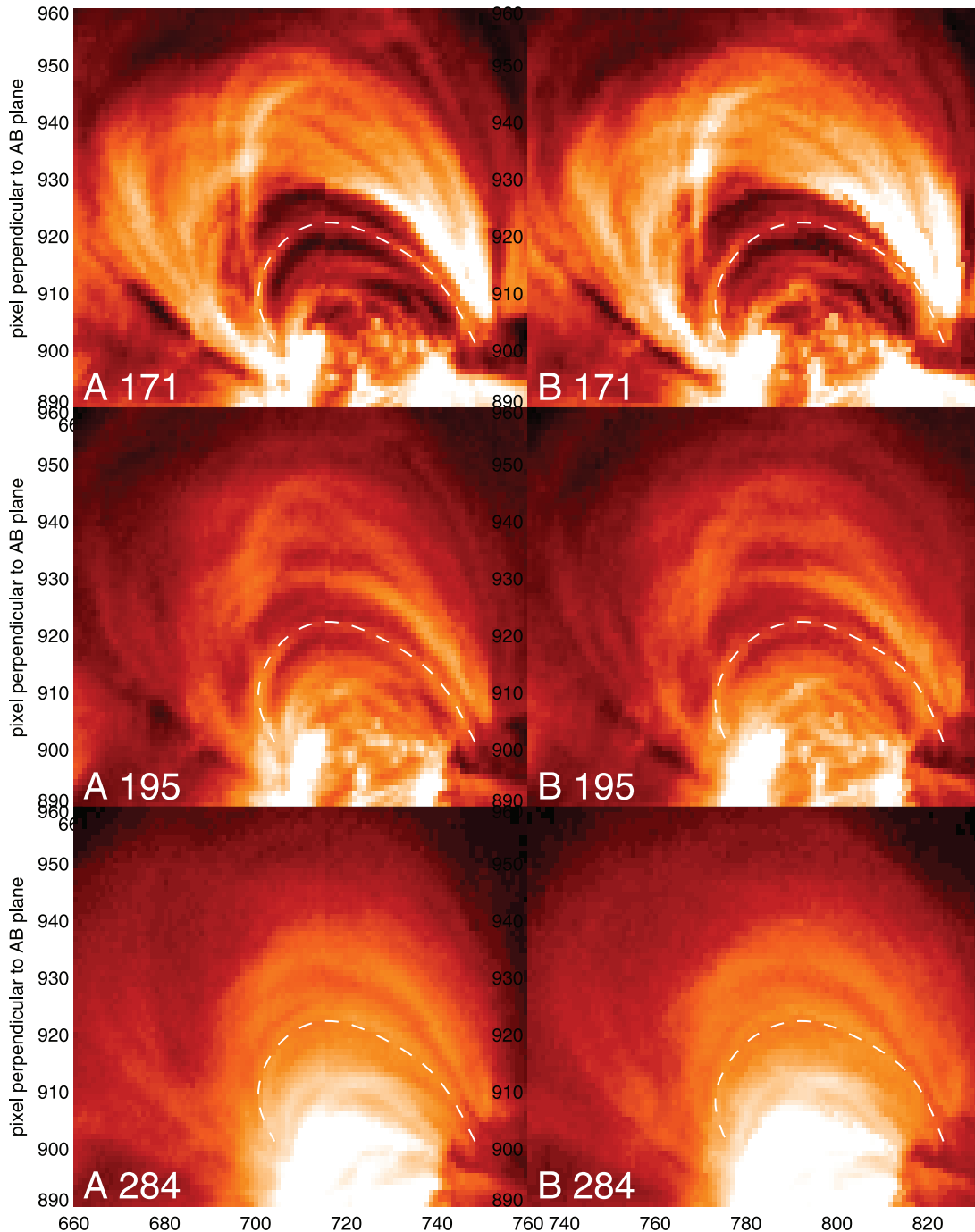
FIG. 1.—Synopsis of six partial images from *STEREO* spacecraft *A* (*left*) and *B* (*right*) in the wavelengths of 171, 195, and 284 Å. The field of view is the *x*-pixel range = [660,760] for *A* (or [732, 832] for *B*) and the *y*-pixel range = [890, 960], with the axes parallel and perpendicular to the spacecraft *AB* plane. The color scale is logarithmic. The overplotted loop (*dashed white curve*) corresponds to loop 3 in Paper I (Aschwanden et al. 2008).

crucial aspect is how the background flux is defined, because the loop-associated flux is defined by the difference of the total flux minus the background flux, i.e., $f_{\mathrm{loop}}(x,y) = f_{\mathrm{total}}(x,y) - f_{\mathrm{back}}(x,y)$ at each loop position $[x(s), y(s)]$, where s is the coordinate along the loop axis. Because it turns out that the loop-associated flux amounts typically only to about $\lesssim 10\%$ of the total flux, we are dealing with a difference of two large quantities (total flux minus background flux), and thus the accuracy of any background subtraction method has to be about 10 times better than the aimed accuracy in the derivation of loop-associated parameters, a fact that was often not appreciated in previous studies.

The key of a sensible method to extract loop-associated EUV or soft X-ray fluxes from the overwhelming background corona is to determine the loop-associated background *as close as possible to the loop*, rather than far away at a dark position of the image. Moreover, since we are only interested in the finest loop structures that an instrument can observe, the background has to be evaluated as close to the loop axis as the instrumental point-spread function allows. For typical EUV images the point-spread function has a FWHM of ≈ 2 pixels, which is a lower limit of the FWHM of unresolved loop structures, and thus the background has to be evaluated $\gtrsim \pm 2$ pixels away from the loop axis. In a simplest model we can consider the loop cross section as a triangular
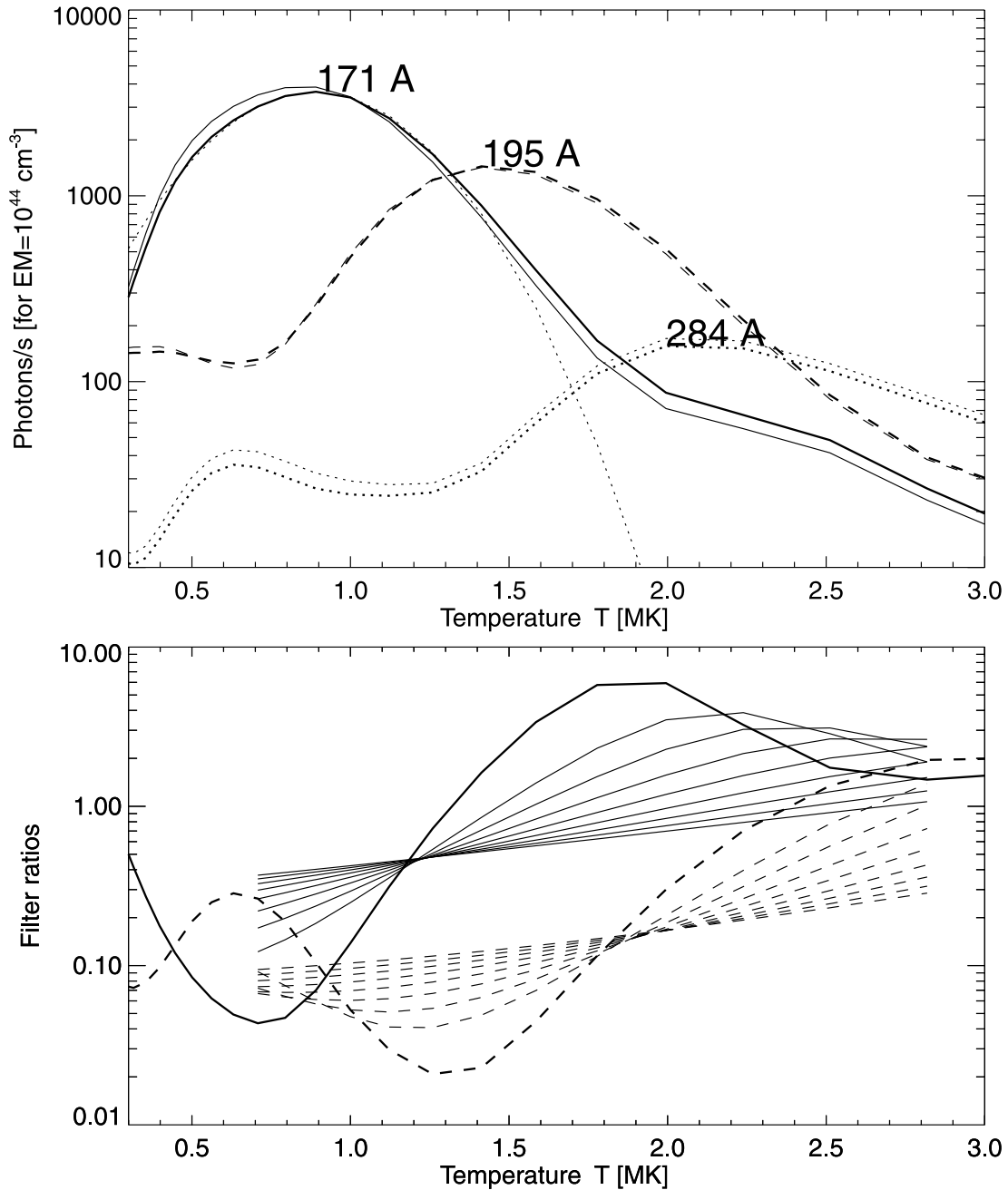
Fig. 2.—*Top*: Response functions of *STEREO* EUVI *A* (*thick curves*) and *B* (*thin curves*) of the 171 Å (*solid curve*), 195 Å (*dashed curve*), and 284 Å (*dotted curve*). The response functions were calculated with the CHIANTI code, using the Feldman abundances and the ionization equilibrium of Mazzotta et al. (1998). The Gaussian width of the 171 Å response function is $\sigma_{171} \approx 0.30$ MK (*dotted Gaussian curve*). *Bottom*: Filter ratios 195/171 (*thick solid curve*) and 284/195 (*thick dashed curve*) for an isothermal DEM ($\sigma_{\rm DEM} = 0$) and for DEMs with Gaussian widths of $\sigma_{\rm DEM} = 0.2, 0.3, \ldots, 1.0$ MK (*thin solid and dashed curves*).

shape with a FWHM of 2 pixels and a flat background. The base of the triangular cross section is thus 4 pixels wide, and in order to have an equal amount of information available for background modeling it is suitable to choose an 8 pixel wide image section across the loop. In our analysis we therefore extract a curved stripe along the loop axis with a width of 8 pixels and a length of $n_s \approx L/\Delta x$ pixels that approximately corresponds to the loop length L divided by the image pixel size Δx (Fig. 3). Let us denote the loop-aligned curved coordinate system with a length coordinate s and a perpendicular coordinate t. The flux values $f_{\rm total}(s_i, t_j)$ for $i = 1, \ldots, n_s; j = -n_w/2, \ldots, +n_w/2$ are evaluated at the Cartesian image positions $[x(s_i, t_j), y(s_i, t_j)]$ by bilinear interpolation. The coordinate grid $[s, t]$ of the curved array with respect to the image

coordinate grid $[x, y]$ is illustrated in Figure 3. We traced individual loops with 4–10 spline points in Paper I, which we interpolate with $n_s \approx 10$–100 positions s_i along the loop axis to map out their length ($L \approx 30$–240 Mm) with a resolution of about an image pixel size.

Even when the background is chosen as close as possible to the loop axis, the evaluation or modeling of the background across a loop cross section profile is still a kind of an art, and we will demonstrate the subtleties of various background definitions in the following. In most of the following experiments we deal with an 8 pixel wide loop cross section, which is defined from the flux profiles at nine positions, i.e., $f(t_j), j = -4, \ldots, +4$, with the loop axis centered at the midpoint t_0. Thus, we have a "left-hand"
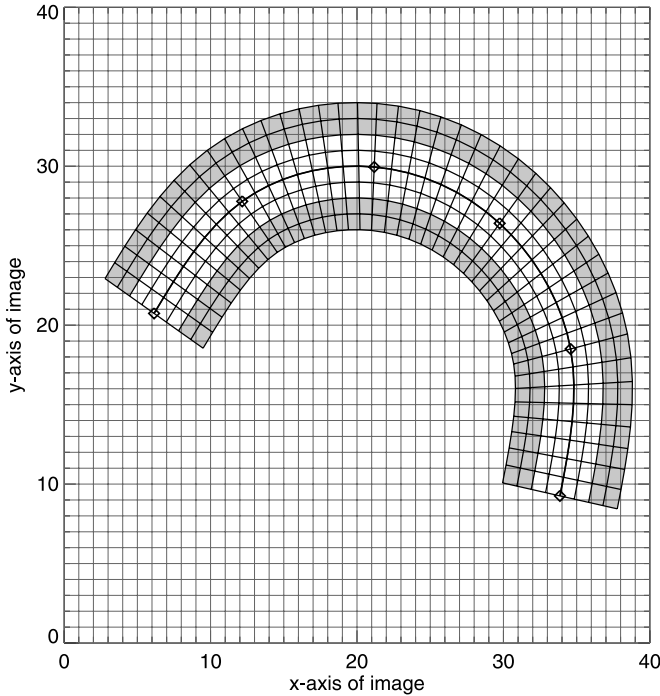
FIG. 3.—Loop-aligned curved coordinate system (s, t) (with dimensions $n_s = 43$ and $n_w = 8$) overlaid on the Cartesian coordinate system (x, y) (with dimensions $n_x = 40$ and $n_y = 40$) of the image. The loop axis is defined by six spline points (*diamonds*) and is interpolated to $n_s = 43$ points s_i on the loop axis t_0. The loop background is evaluated at the location of the central loop cross section ($|t - t_0| \leq 2$) from the boundary zones on the left- and right-hand sides ($2 \leq |t - t_0| \leq 4$), both marked with gray areas. Note that the pixel size in the curved array is commensurable with the pixel size of the Cartesian grid.

background section at ($t_{-4} \leq t \leq t_{-2}$), a loop middle section at ($t_{-2} \leq t \leq t_{+2}$), and a "right-hand" background section at ($t_{+2} \leq t \leq t_{+4}$). In a first method (P0; see explanation of acronyms P0–P3, C0–C1, S1–S3, and CG in Fig. 4) we interpolate the background just linearly between the closest bracketing background points (between t_{-2} and t_{+2}), which would bracket a triangular cross section with a base width of 4 pixels or a FWHM of 2 pixels (corresponding to the instrumental resolution). In a second method we perform a low-order polynomial fit through the left and right background zones by linear (P1), quadratic (P2), or cubic (P3) polynomial fitting to the fluxes (at the six background pixels). The cubic polynomial fitting method (P3) has also been applied to *SOHO* EIT data (Aschwanden et al. 1999, 2000a). In a third method (CG), that especially reinforces the cospatiality between the three filters, a cospatial fit of a linear background profile plus a Gaussian loop profile is performed, which requires 11 free parameters and has been successfully applied to *TRACE* data (Aschwanden & Nightingale 2005). We explore a fourth method (S1, S2, and S3) that involves a larger environment than the 8 pixel wide loop stripe for background modeling, in defining a global background image by smoothing the full image with a boxcar of 3×3 (S1), 5×5 (S2), or 7×7 pixels (S3). An example for each of the 10 different background definition methods is shown in Figure 4, where it can be seen that they exhibit considerable differences in the determination of the loop-associated fluxes (see discussion in § 3.1).

2.4. *Differential Emission Measure (DEM) Modeling*

For electron temperature $T_e(s)$ and electron density $n_e(s)$ modeling we approximate the differential emission measure

(DEM) distribution with a Gaussian function (for each loop position s),

$$\left[\frac{d\,\mathrm{EM}(T)}{dT} \right](s)\,dT = \mathrm{EM}_p(s)\exp\left\{ -\frac{[T - T_p(s)]^2}{2\sigma_{\mathrm{DEM}}^2(s)} \right\}, \quad (1)$$

where $\mathrm{EM}_p(s)$ is the peak emission measure at the DEM peak temperature $T_p(s)$ and $\sigma_{\mathrm{DEM}}(s)$ is the Gaussian (half) width of the DEM function. We are using the EUVI response functions $R_{171}(T)$, $R_{195}(T)$, and $R_{284}(T)$, as shown in Figure 2 (*top panel*), and perform a forward fit of the DEM function (eq. [1]) to the three background-subtracted fluxes (at loop length position s and loop axis midpoint position $t = t_0$) to obtain the best-fit values $\mathrm{EM}_p(s)$, $T_p(s)$, and $\sigma_{\mathrm{DEM}}(s)$ of the DEM distribution, i.e.,

$$f_{171}(s, t_0) - b_{171}(s, t_0) = \int \frac{d\,\mathrm{EM}(T)}{dT}(s)R_{171}(T)\,dT, \quad (2)$$

$$f_{195}(s, t_0) - b_{195}(s, t_0) = \int \frac{d\,\mathrm{EM}(T)}{dT}(s)R_{195}(T)\,dT, \quad (3)$$

$$f_{284}(s, t_0) - b_{284}(s, t_0) = \int \frac{d\,\mathrm{EM}(T)}{dT}(s)R_{284}(T)\,dT. \quad (4)$$

The resulting temperature profile $T_p(s)$ represents the temperature T_p at the peak of the DEM distributions, while the full DEM distribution has a Gaussian half-width of $\sigma_{\mathrm{DEM}}(s)$.

2.5. *Electron Density Profiles*

To obtain the electron density profile $n_e(s)$ we have first to measure the loop width w. From the background-subtracted cross-sectional flux profile we define a loop width $w(s)$ by the equivalent width of the integrated loop cross section,

$$w(s) = \left\{ \frac{\int_{t_{b1}}^{t_{b2}} [f_\lambda(s, t) - b_\lambda(s, t)]\,dt}{\max[f_\lambda(s, t) - b_\lambda(s, t)]} \right\}, \quad (5)$$

where the integration limits are the left boundary ($t_{b1} = t_{-2}$) and the right boundary ($t_{b2} = t_{+2}$). The wavelength λ is chosen by the filter in which the loop is brightest. Since the variation of the loop width $w(s)$ is small along the loops and is mostly affected by uncertainties of the background subtraction, we use only the average width $w = \langle w(s) \rangle$ in the following density estimates.

The electron density $n_e(s)$ is then calculated, assuming optically thin emission (as is generally the case for the solar corona in EUV and soft X-ray wavelengths), from the peak emission measure value EM_p evaluated at the loop axis ($t = t_0$) and the loop width w by

$$n_e(s) = \sqrt{\frac{\mathrm{EM}_p(s)}{wA}}, \quad (6)$$

where EM_p (cm^{-3}) is the emission measure per volume unit and $A = 1.33 \times 10^{16}\ \mathrm{cm}^2$ is the square area of an EUVI pixel (with a pixel size of 1.59″).

Since the width of the measured loops is close to the instrumental resolution of $w_{\mathrm{res}} = 2$ pixels, we estimate an effective loop width by adding the corrected loop width w_c and the width of the point-spread function w_{res} in quadrature,
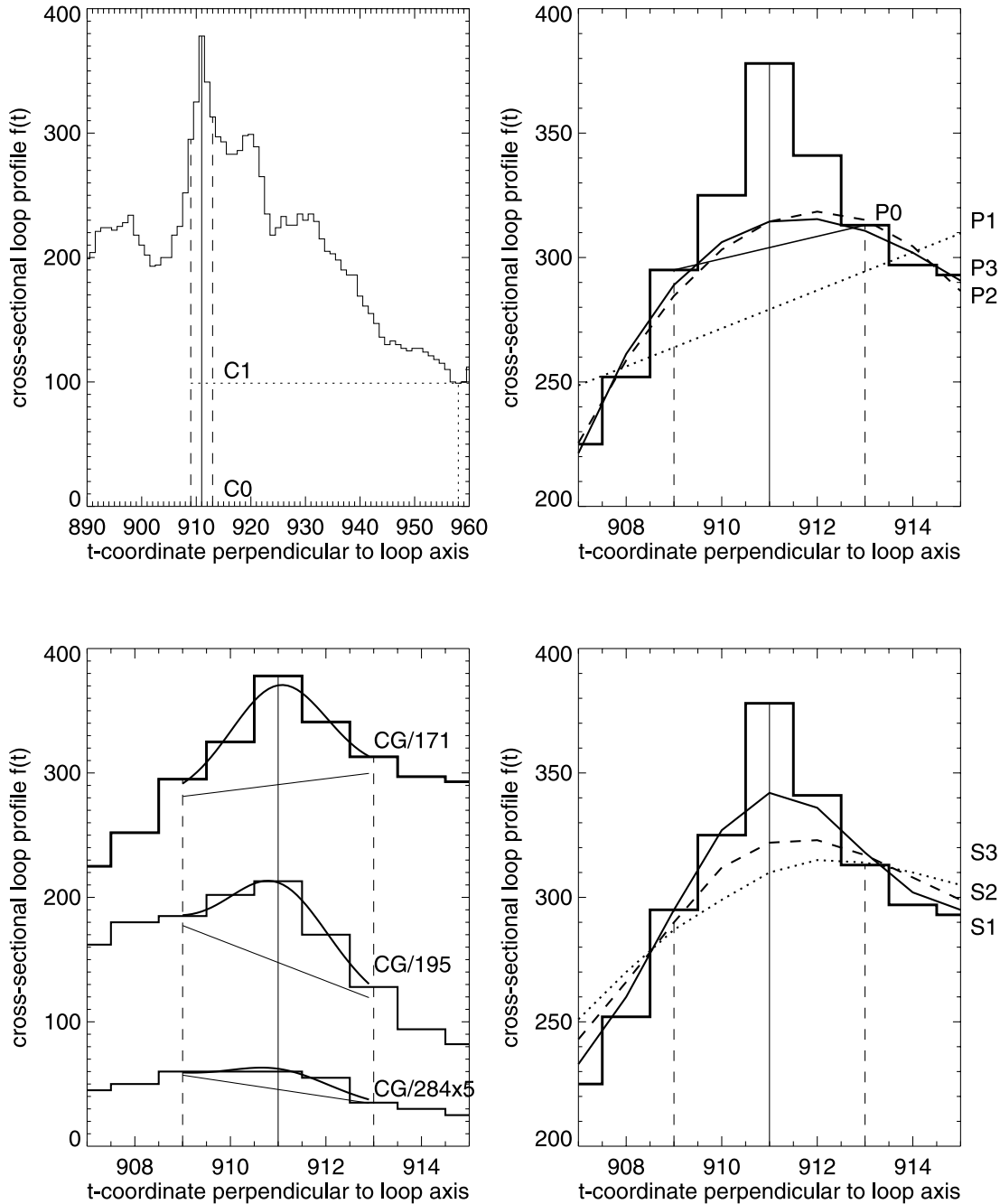
$$w_c(s) = \sqrt{w(s)^2 - w_{\mathrm{res}}^2}, \quad (7)$$

FIG. 4.—The 10 different background subtraction methods are illustrated for an image stripe at position $x = 720$, $y = 890$–960 in *STEREO B*, with a loop cross section centered at position $y_0 = 911$. *Top left*: C0 = no background subtraction, C1 = background evaluated from lowest brightness in local subimage. *Top right*: P0 = Linear interpolation between loop boundaries (at $y = 909$ and $y = 913$); P1 = linear, P2 = quadratic, and P3 = cubic polynomial fit to boundary zones ($y = 907$–909 and $y = 913$–915). *Bottom left*: CG = Cospatial fit of Gaussian loop profile plus linear background simultaneously in all three temperature filters. The flux in the 284 Å filter is multiplied by a factor of 5 in the display. *Bottom right*: S1 = 3×3 boxcar, S2 = 5×5 = boxcar, and S3 = 7×7 boxcar smoothing of image. The physical parameters resulting from these 10 different background subtraction methods are given in Table 2.

which introduces the following correction for the inferred electron density,

$$n_{e,c}(s) = n_e(s) \sqrt{\frac{w(s)}{w_c(s)}}. \qquad (8)$$

3. RESULTS

The quantitative results of our data analysis of 30 loops are described in this section. The 3D geometry of these 30 loops is derived in Paper I, while we focus here on the measurement of their electron temperatures, electron densities, and loop widths. Since the method of background subtraction is most crucial for the outcome of these physical parameters, we also present test results from 10 different background definition methods in § 3.1 to justify our choice of the most suitable method.

3.1. *Evaluation of Background Subtraction Methods*

We applied the 10 background subtraction methods, described in § 2.3 and illustrated in Figure 4, to a number of stereoscopically reconstructed loops and document a comparison of their performance for the particular case of loop 3 here (Table 2 and Figs. 5–7).

TABLE 2
EVALUATION OF 10 BACKGROUND-SUBTRACTION METHODS FOR LOOP NO. 3

Background Subtraction Method (1)	Spacecraft *STEREO* (2)	Completeness Fraction q_{comp} (3)	DEM Peak Temperature T_p (MK) (4)	DEM Width σ_{DEM} (MK) (5)	Loop Flux Ratio q_{loop} (6)	Loop Width w (Mm) (7)	Loop Density n_A (cm^{-3}) (8)	Density Ratio n_B/n_A (9)
C0.......................	A	1.00	1.76 ± 0.14	0.93 ± 0.11	1.00	4.9	2.13×10^9	0.98
C1.......................	A	1.00	2.02 ± 0.23	0.86 ± 0.15	0.65	4.3	2.04×10^9	1.00
P0	A	0.98	1.23 ± 0.26	0.38 ± 0.18	0.18	2.4	1.77×10^9	0.92
P1	A	0.84	1.21 ± 0.30	0.36 ± 0.18	0.17	2.7	1.82×10^9	0.90
P2	A	0.98	1.16 ± 0.18	0.40 ± 0.22	0.21	2.9	1.76×10^9	0.97
P3	A	0.98	1.16 ± 0.18	0.40 ± 0.22	0.21	2.8	1.79×10^9	0.94
CG	A	0.98	1.25 ± 0.28	0.41 ± 0.19	0.21	2.9	1.73×10^9	0.96
S1	A	0.94	1.24 ± 0.34	0.41 ± 0.24	0.05	1.9	1.10×10^9	0.89
S2	A	0.98	1.22 ± 0.39	0.46 ± 0.23	0.10	2.0	1.43×10^9	0.94
S3	A	0.88	1.18 ± 0.31	0.44 ± 0.22	0.12	2.1	1.57×10^9	0.90

We have subdivided the length of loop 3 into $n_s = 51$ positions along the loop. Images of loop 3 in all three wavelengths and from both spacecraft A and B are shown in Figure 1, and the loop flux cross sections at the $2 \times 3 \times 51$ positions are plotted in Figure 5, extracted from a curved array with dimensions $n_w = 9$ and $n_s = 51$, as illustrated in Figure 3. Figure 5 shows the application of one particular background subtraction method, namely, the cubic polynomial fit method (P3), which fits the background in the zones that are $\pm 2, \ldots, 4$ pixels away from the loop axis. One quality measure of background subtraction methods is the completeness fraction $q_{frac} = n_{s1}/n_s$, defined by the number n_{s1} of loop cross sections where the background subtraction yields a physical solution, i.e., a positive loop flux, $f_{loop}(s) > f_{back}(s)$. This *completeness fraction* (see Table 2, col. [3]) is $q_{comp} = 1.00$ for the case of no background subtraction (C0) or subtraction of a too low background, such as the darkest area in the image (C1). Among the other eight methods, the best value is $q_{comp} = 0.98$, which means that they miss only one cross section out of the $n_s = 51$ positions. In Figure 5 we see that the only cross section with an unphysical solution is the last loop position (displayed as topmost cross sections in Fig. 5), which corresponds to the eastern footpoint of the loop. Therefore, we can consider all other methods with $q_{comp} = 0.98$ as equally successful, such as P0, P2, P3, CG, and S2. This completeness fraction is drastically lower for the same loop observed with *STEREO B*. The reason is simply that *STEREO B* samples the background from a different direction, where a secondary much brighter loop emerges at the right-hand background in the 171 and 195 Å images, which makes it impossible for any background subtraction method to extract the weaker target loop properly in the first 15 loop positions (see near the bottom of the fourth and fifth panels in Fig. 5). Anyway, the other methods with a lower completeness fraction (Table 2, col. [3]), i.e., $q_{comp} = 0.84$ for P1, $q_{comp} = 0.94$ for S1, and $q_{comp} = 0.88$ for S3, have a similar problem in modeling the background in the first 15 loop positions seen from spacecraft A because they produce an almost linear background and cannot adapt to different slopes of the background on the left and right side of the loop cross sections. Clearly, higher order polynomials (P2 and P3) are more capable of adjusting to such asymmetric backgrounds with different slopes on both sides.

Another useful parameter of evaluating the quality of the background subtraction methods is the loop flux ratio q_{loop} and the loop width w (eq. [5]). We define the loop flux ratio q_{loop} by

adding the loop-associated fluxes in each loop position s and wavelength λ,

$$q_{loop} = \frac{\sum_{s,\lambda}[f_\lambda(s) - b_\lambda(s)]}{\sum_{s,\lambda}[f_\lambda(s)]}. \qquad (9)$$

We list these quantities in Table 2 (col. [6]). In the case of no background subtraction we have of course $q_{loop} = 1.00$, and similarly high for the case of a too low background subtraction, e.g., $q_{loop} = 0.65$ by choosing the darkest part in the image. For all other methods we have significantly smaller fractions in the range of $0.05 \leq q_{loop} \leq 0.21$. We see that the high-pass filter with the smallest boxcar of 3×3 (S1) snugs too close to the peak and captures only 5% of the flux and also produces the smallest loop width of $w = 1.90$ Mm (1.6 EUVI pixels) below the spatial resolution (2 EUVI pixels). In addition, the other high-pass filters capture significantly less flux ($q_{loop} = 0.10$–0.12) and yield a smaller loop width ($w = 2.0$–2.1 Mm) than the others.

This evaluation leaves us with the methods P0, P2, P3, and CG as winners with equally good performance. All of these four methods yield a completeness fraction of $q_{comp} = 0.98$, a loop flux of $q_{loop} = 0.20 \pm 0.02$, and a loop width of $w = 2.8 \pm 0.2$ Mm. From also studying other cases we find that a higher order polynomial such as P3 is generally superior because it can better adjust to asymmetric backgrounds with different slopes. Even the method of cospatial fits of a Gaussian with a linear background, although it has the advantage of reinforcing the cospatiality in different filters, often does not have enough flexibility to model a nonlinear background, the main reason for the 80% of cases with insufficient goodness of fit in the *TRACE* study of Aschwanden & Nightingale (2005). Therefore, we adopt the background subtraction method P3 in the following, which fits the background zones with a polynomial of third order as was previously also applied for 60 coronal loops observed with *SOHO* EIT (Aschwanden et al. 1999, 2000a).

The cross-sectional fits of the background subtraction method P3 are shown in Figure 5, and the resulting background profiles $f_{\lambda,back}$ are shown in Figure 6 for both the A and B spacecraft. The resulting flux ratios are $q_{loop}^A = 0.21$ for A and $q_{loop}^B = 0.13$ for B. We emphasize that these ratios are not expected to be equal, because each spacecraft sees the background in a different direction, but a background flux of order 90%, or a loop-associated flux of order $\approx 10\%$, is very typical for EUV data. Background subtraction methods that subtract out significantly less background
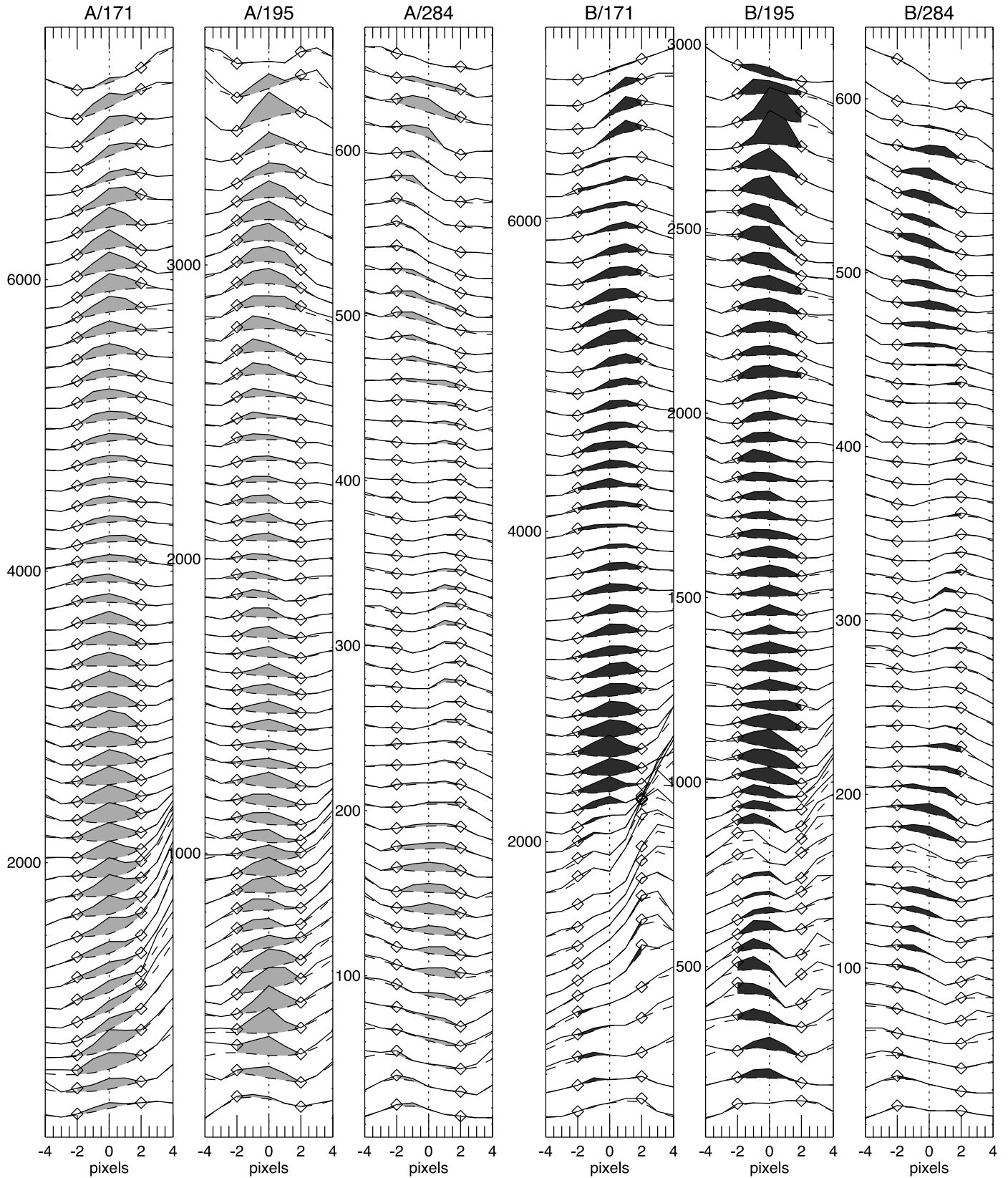
FIG. 5.—Cross-sectional loop profiles for loop 3 (marked in Fig. 1) at $n_s = 51$ positions along the loop, where the western footpoint position corresponds to the lowest displayed profile, while the profiles of the subsequent positions are incrementally shifted by a constant offset. The six panels contain the cross-sectional profiles from the three wavelength filters (171, 195, 284 Å) from both the A (*left half*) and B spacecraft (*right half*). The background profile is defined by a cubic polynomial fit to the fluxes of the pixels ($-4, -2$) and ($2, 4$), while the background-subtracted loop flux is indicated with a colored area. [*See the electronic edition of the Journal for a color version of this figure.*]
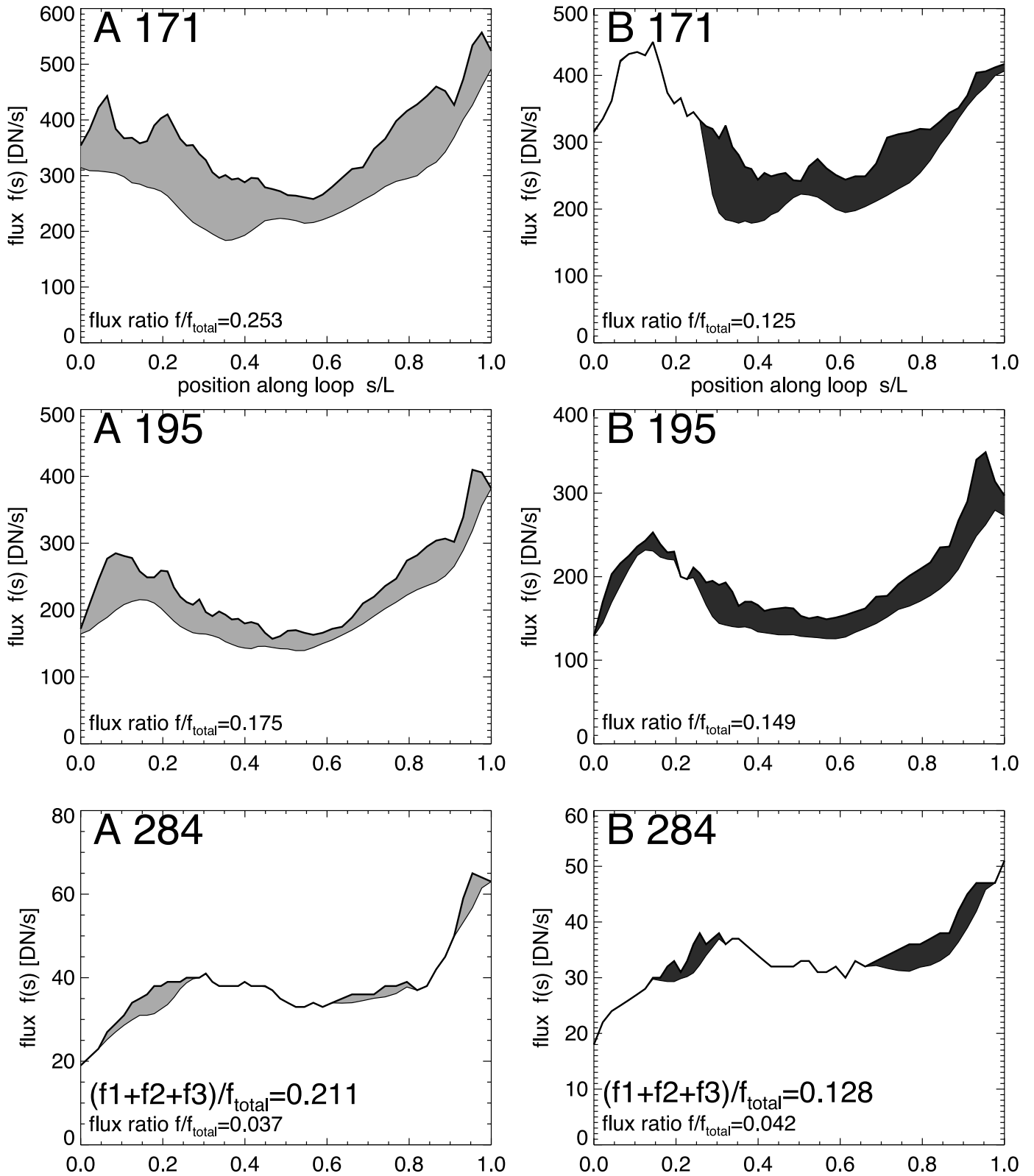
FIG. 6.—Flux profiles $f(s)$ (*thick line*) of loop 3 along the loop coordinate s, for each filter (*top left*: 171 Å, *middle left*: 195 and 284 Å) and for the EUVI *A* (*left*) and EUVI *B* spacecraft (*right*). The background is evaluated with the cubic polynomial fit method as shown in Fig. 5. The background-subtracted loop fluxes are indicated with colored areas. [*See the electronic edition of the Journal for a color version of this figure.*]
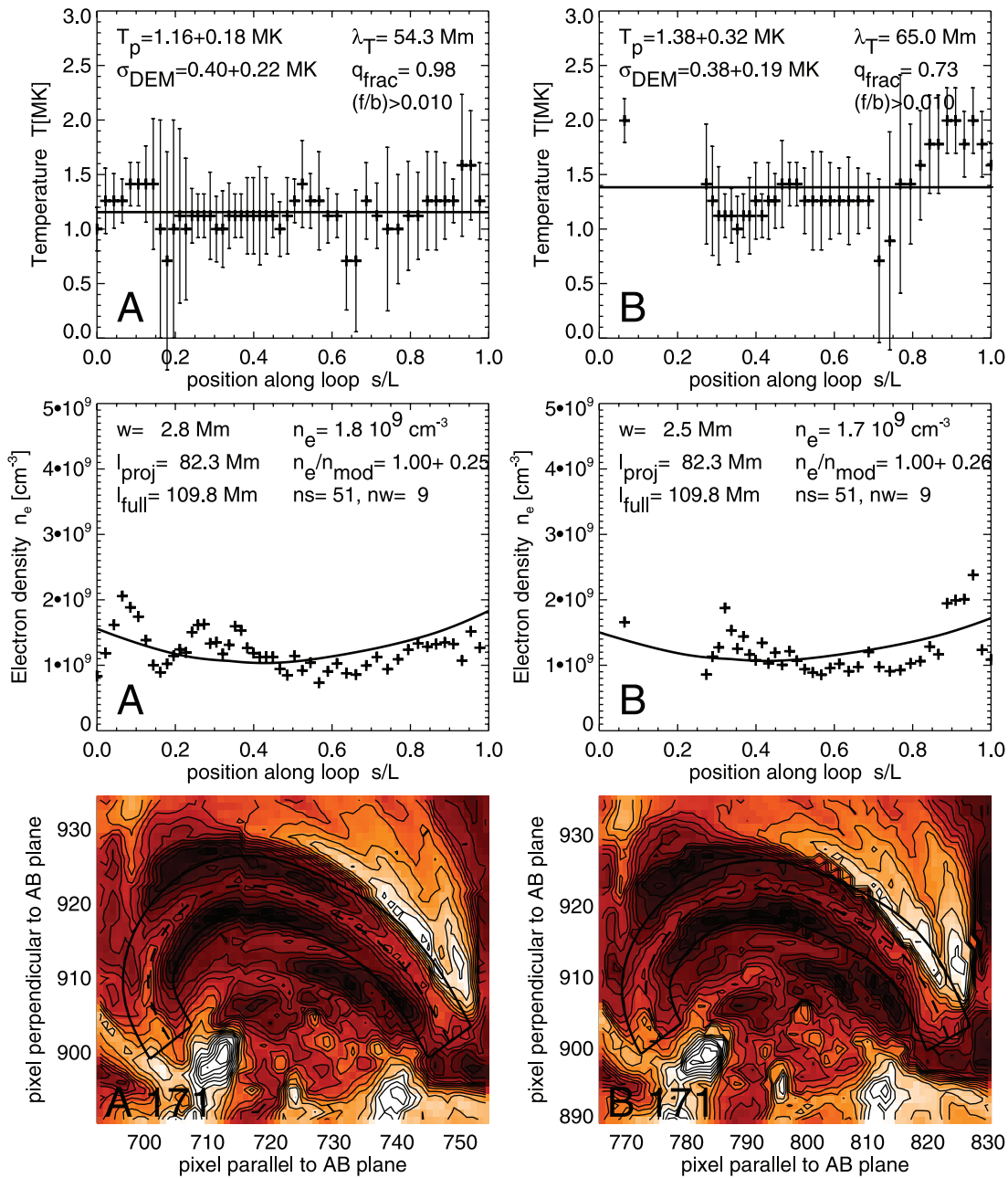
Fig. 7.—Temperature profiles $T_e(s)$ (top), electron density profiles $n_e(s)$ (middle), and partial maps containing loop 3 (bottom) for both spacecraft STEREO A (left) and B (right). The temperature profiles contain the DEM peak temperature $T_p(s)$ and the Gaussian DEM widths (vertical bars). The major gap at $s/L \lesssim 0.25$ in spacecraft B results from the failure of the background subtraction method due to a closely spaced, bright loop. The horizontal line in the temperature profile indicates the mean temperature, and the curve in the density profile corresponds to a hydrostatic density model with a temperature scale height λ_T predicted by the mean loop temperature $\langle T_p \rangle$.

are likely to be heavily contaminated by the fore- and background corona.

3.2. Self-Consistency between Spacecraft STEREO A and B

This is the first time that we have two identical instruments in space that independently measure physical parameters of coronal loops. At small stereoscopic separation angles, the fluxes measured with both spacecraft could be used for cross-calibration. At larger separation angles, each spacecraft measures a different total flux for a given coronal loop, because the background flux is integrated along two different lines of sight. The temperature profiles $T_e(s)$ and density profiles $n_e(s)$ measured for loop 3 are shown for both spacecraft A and B in Figure 7, based on the background-subtracted fluxes shown in Figure 6. A major difference is that a closely spaced loop in the first quarter section of the loop (at

$s/L \lesssim 0.25$, starting from the western footpoint) affects the background subtraction differently for the STEREO A and B spacecraft. With STEREO A we barely manage to model this bright secondary loop as part of the background using the cubic spine polynomial fit method, but we fail to retrieve the loop flux with STEREO B because the secondary loop is seen closer to the loop axis of the primary loop for the stereoscopic angle of B (see cross-sectional profiles in Fig. 5). A consequence is that B cannot measure temperature and density in this loop section. Apart from this problem there also seems to be an interfering hotter loop to be present in 284 Å that is picked up by STEREO B in the loop section near the eastern footpoint ($s/L \gtrsim 0.8$; see Fig. 7, top right). All these differences result into a slightly higher average loop temperature of $T_p = 1.38 \pm 0.32$ for STEREO B than $T_p = 1.16 \pm 0.18$ for STEREO A (Fig. 7, top). However, for the average density we find very good
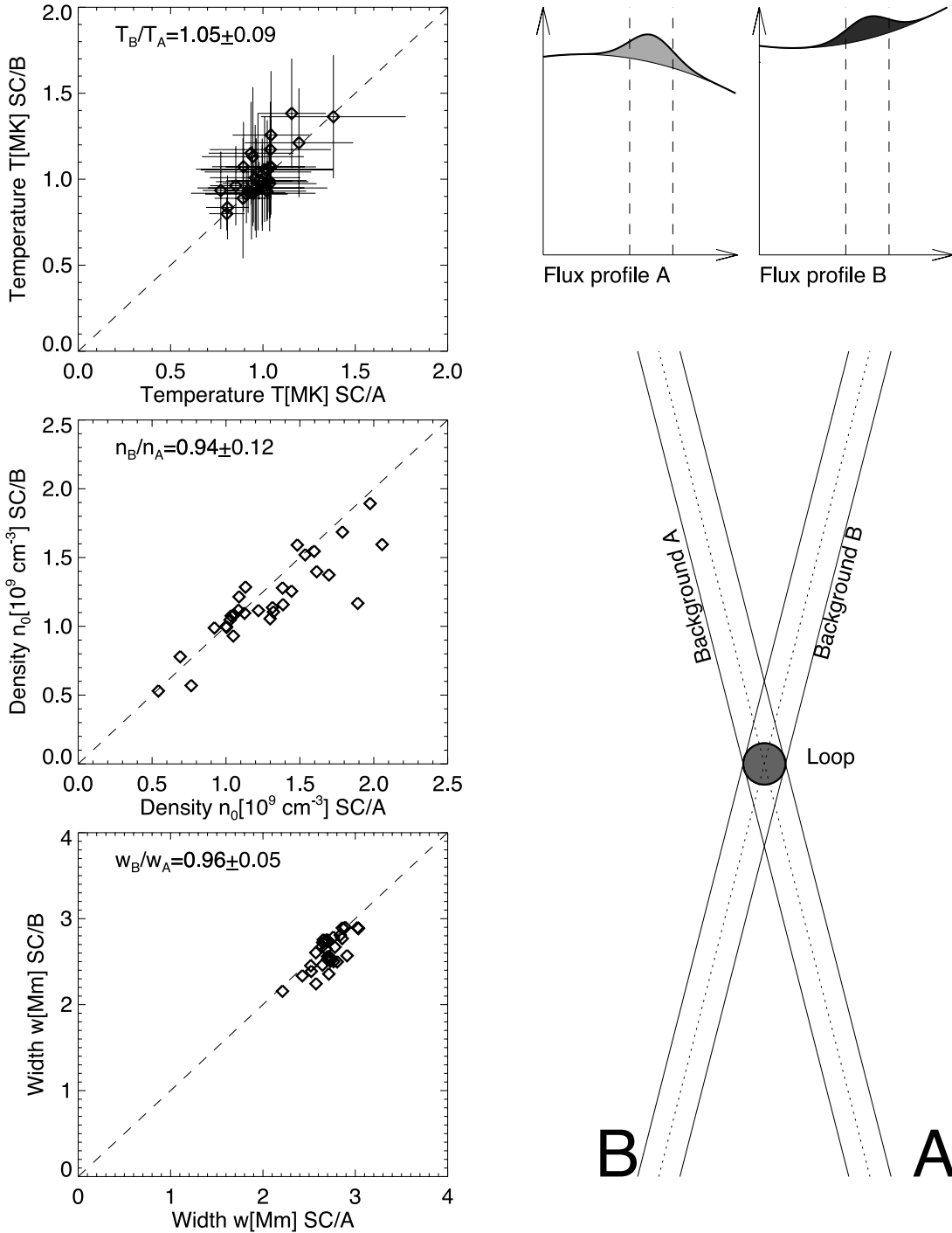
Fig. 8.—Self-consistency of mean loop temperatures T_A, T_B (top left), base electron densities n_A, n_B (middle left), and mean loop widths w_A, w_B (bottom left) measured with spacecraft STEREO A vs. STEREO B. These loop parameters are inferred from the background-subtracted loop-associated flux (top right), based on independent background subtractions for the different lines of sight of both spacecraft A and B (bottom right). [See the electronic edition of the Journal for a color version of this figure.]

agreement (within 5%) between the two spacecraft, with a loop base density of $n_A = 1.8 \times 10^9$ cm^{-3} for A and $n_B = 1.7 \times 10^9$ cm^{-3} for B (see Fig. 7, middle panels).

From these detailed studies of the differences in T_e and n_e diagnostics between the two spacecraft STEREO A and B it is clear that most of the differences result from background subtraction issue, rather than from other uncertainties such as Poisson count noise or DEM modeling. Other uncertainties, such as assumptions of atomic elemental abundances or the ionization equilibrium, cancel out in the nearly identical response functions of

STEREO A and B (Fig. 2). One has to be aware that the background flux seen by the two spacecraft does not only sample different parts of the solar corona (see sketch in Fig. 8, right), but is also about 10 times larger than the flux of the analyzed (finest) loops, and thus a 1% error in the background subtraction causes a 10% error in loop quantities. Nevertheless, if we compare all mean loop temperatures T_A of the 30 analyzed loops measured with STEREO A with those (T_B) from STEREO B, we find quite good agreement of $T_B/T_A = 1.05 \pm 0.09$ (Fig. 8, top left). A similar good agreement is found for the loop base densities

TABLE 3
PHYSICAL PARAMETERS OF SEVEN COMPLETE LOOPS

Loop/Spacecraft No. (1)	Inclination Angle (deg) (2)	Height Max. h (Mm) (3)	Loop Full Length $2L$ (Mm) (4)	Loop Width $w,(w_c)$ (Mm) (5)	Loop Flux Ratio $f_{\rm loop}/f_{\rm total}$ (6)	DEM Peak Temperature T_p (MK) (7)	DEM Width $\sigma_{\rm DEM}$ (MK) (8)	Base Density $n_0,(n_{0c})$ (10^9 cm^{-3}) (9)	Density Model Fit $n/n_{\rm model}$ (10)	Loop Fraction $q_{\rm frac}$ (11)
1 A.................	51.3	11.6	59.4	2.5 (1.0)	0.118	1.38 ± 0.39	0.39 ± 0.23	1.54 (2.42)	1.00 ± 0.38	0.61
1 B.................				2.5 (0.8)	0.091	1.36 ± 0.36	0.38 ± 0.25	1.52 (2.60)	1.00 ± 0.41	0.55
2 A.................	56.7	10.9	68.4	2.4 (0.8)	0.106	1.20 ± 0.29	0.32 ± 0.16	1.22 (2.18)	1.00 ± 0.30	0.67
2 B.................				2.3 (0.4)	0.073	1.21 ± 0.32	0.30 ± 0.17	1.12 (2.78)	1.00 ± 0.34	0.51
3 A.................	35.7	29.8	109.8	2.8 (1.5)	0.211	1.16 ± 0.18	0.40 ± 0.22	1.79 (2.41)	1.00 ± 0.25	0.98
3 B.................				2.5 (1.0)	0.128	1.38 ± 0.32	0.38 ± 0.19	1.69 (2.71)	1.00 ± 0.26	0.73
4 A.................	42.9	30.7	127.4	2.7 (1.4)	0.172	1.04 ± 0.19	0.32 ± 0.15	2.06 (2.85)	1.00 ± 0.31	0.82
4 B.................				2.5 (1.0)	0.115	1.07 ± 0.30	0.34 ± 0.16	1.60 (2.50)	1.00 ± 0.36	0.79
5 A.................	72.8	13.0	121.8	2.6 (1.3)	0.098	1.04 ± 0.24	0.34 ± 0.17	1.13 (1.61)	1.00 ± 0.36	0.79
5 B.................				2.5 (0.9)	0.076	1.07 ± 0.28	0.36 ± 0.19	1.10 (1.85)	1.00 ± 0.34	0.61
6 A.................	58.6	26.2	157.3	2.8 (1.6)	0.091	0.91 ± 0.22	0.30 ± 0.18	1.31 (1.74)	1.00 ± 0.37	0.52
6 B.................				2.5 (1.0)	0.067	0.91 ± 0.17	0.36 ± 0.19	1.14 (1.83)	1.00 ± 0.47	0.41
7 A.................	69.0	32.2	266.6	2.7 (1.4)	0.071	0.95 ± 0.34	0.41 ± 0.27	1.00 (1.37)	1.00 ± 0.42	0.41
7 B.................				2.6 (1.1)	0.065	0.92 ± 0.17	0.32 ± 0.19	1.00 (1.52)	1.00 ± 0.56	0.27
A+B.................	55	22	130	2.6 (1.1)	0.106	1.11	0.35	1.4 (2.17)	0.37	0.62
	± 13	± 9	± 67	± 0.14 (± 0.3)	± 0.042	± 0.17	± 0.04	± 0.3 (0.51)	± 0.09	± 0.19

n_A from *STEREO A* and n_B from *STEREO B*, namely, $n_e = 0.94 \pm 0.12$ (Fig. 8, *middle left*), although the base densities vary by about a factor of 4 between different loops. In addition, the inferred loop widths w_A from *STEREO A* and w_B from *STEREO B* agree within $w_B/w_A = 0.96 \pm 0.05$. So, we can claim an agreement of the order of a few percent for all these mean loop parameters as measured independently by the two spacecraft.

3.3. *Electron Temperatures*

From the three-parameter DEM model (a Gaussian as specified in eq. [1]) we determined the DEM peak temperature T_p and the DEM width $\sigma_{\rm DEM}$ for all 30 loops (and for 10–100 loop positions in each loop), for both the *STEREO A* and *B* spacecraft. An example of the temperature values $T_p(s)$ along a loop (No. 3) is shown in Fig. 7 (*top*), which has a mean value and standard deviation of $T_p = 1.16 \pm 0.18$ MK for *A* and $T_p = 1.38 \pm 0.32$ MK for *B*. That means that the scatter of DEM peak temperatures is only of the order of $\sigma_T/T_p \approx 0.2$ along the loop. Inquiring about the temperature profiles and cross-sectional background fits of all 30 loops we find no systematic variation of $T_p(s)$ along the loops, except for contaminations by secondary loops in the background that have different temperatures. Thus, we determine here only the means T_p and standard deviations σ_T, which are listed for the seven complete loops in Table 3 and shown in a cross-correlation plot for all 30 loops in Figure 8 (*top left*). So, a first conclusion is that we find mostly isothermal loop temperature profiles within $\lesssim 20\%$, mostly subject to background subtraction uncertainties. Theoretically, we would expect a temperature drop from coronal temperatures $\gtrsim 10^6$ K across the transition region toward chromospheric temperatures of $\approx 10^4$ K, but apparently we cannot resolve this temperature drop near the loop footpoints with the spatial resolution of EUVI (2300 km).

A next interesting result is the absolute value of the DEM peak temperatures T_p found among the 30 loops. Among the seven complete loops we find a variety from a hottest loop with $T_p = 1.38 \pm 0.39$ MK (loop 1*A*) down to a coolest loop with $T_p = 0.91 \pm 0.22$ MK (loop 6*A*), which are significantly different. We show a temperature map of the 30 loops in Figure 9, which features

loop temperatures in the range of 0.89 MK $\leq T_p \leq$ 1.38 MK. Of course, this range of loop temperatures is dictated by the sensitivity range of the 171 Å filter (see Fig. 2), in which all loops were originally traced. This temperature range also has substantial overlap with the sensitivity of the 195 Å filter (see Fig. 2), and thus the loop temperatures are mostly defined by the 195/171 filter ratio (Fig. 2, *bottom*), while the 284 Å filter is very insensitive in this temperature range and serves only as an upper limit constraint for ambiguities in the 195/171 filter ratio. Anyway, an important conclusion is that we can measure significantly different loop temperatures with our triple-filter analysis, consistent with both independent spacecraft *STEREO A* and *B* in loop segments that have no background definition problems.

The temperature map shows a trend that the hottest loops are also the shortest loops and those that are located in the center of the active region, while the larger loops overarching the active region or located at the periphery of the active region tend to be cooler (see Fig. 9).

In our three-parameter DEM model we also determined the width $\sigma_{\rm DEM}$ of the DEM distribution, which comes out typically to $\sigma_{\rm DEM} = 0.35 \pm 0.04$ (Table 3, col. [8]). We have to be aware that the Gaussian width of the 171 Å response function is about $\sigma_{171} = 0.30$ MK, so we do not expect to resolve much narrower DEM widths and limited our forward-fitting algorithm to a minimum value of $\sigma_{\rm DEM, min} \geq 0.2$ MK. A background subtraction error of 10% in one filter would represent a 100% error of the loop-associated flux, which changes the filter ratio by a factor of 2, which is about the difference between the filter ratio of a delta function $\sigma_{\rm DEM} = 0$ and $\sigma_{\rm DEM} = 0.2$ MK, as can be read from Figure 2 (*bottom*). Therefore, we do not consider the difference of our statistical fitting of $\sigma_{\rm DEM} \approx 0.35$ from the intrinsic width of the response function $\sigma_{171} \approx 0.3$ as significant, given the uncertainties of the background subtraction in the DEM fitting, and thus all loops could well be isothermal. It is interesting to note that a similar DEM Gaussian-fitting study with *TRACE* triple-filter data yielded a narrower mean DEM Gaussian width of $\sigma_{\rm DEM} = 0.07 \pm 0.10$ MK, which probably indicates that the 3 times higher spatial resolution of *TRACE* also allows for a better
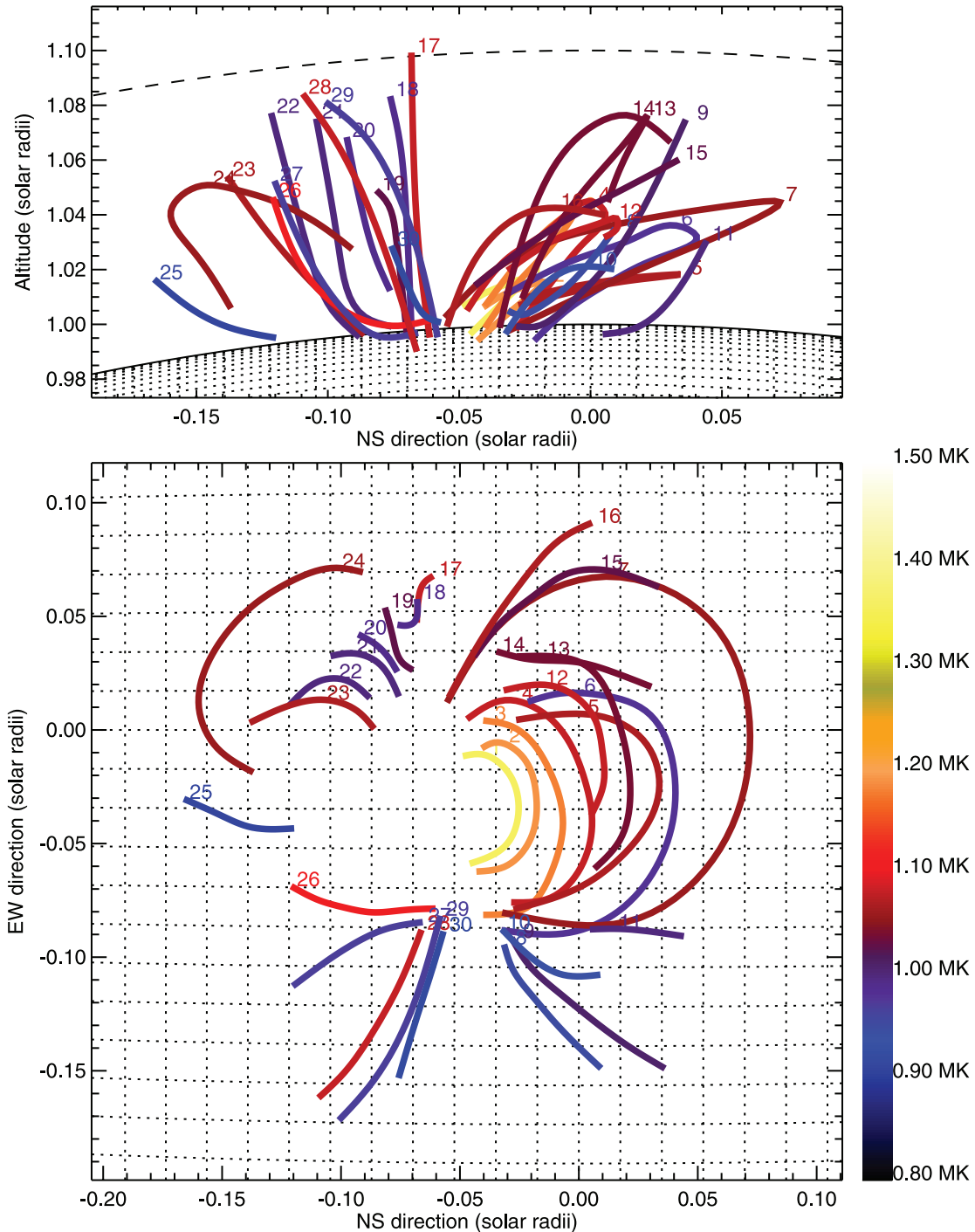
FIG. 9.—Colored temperature map of the 30 analyzed loops in the active region rotated to the limb. The colors represent a temperature scale ranging from 0.8 to 1.5 MK. Note that the hottest loops tend to be the smallest loops located in the center of the active region.

background modeling 3 times closer to the loop axis, which reduces uncertainties in the background-subtracted loop-associated fluxes substantially and therefore yields more accurate filter ratios, temperatures, and DEM widths.

3.4. *Electron Densities*

The three-parameter DEM model provides the emission measure $EM_p = EM(T = T_p)$ at the DEM peak temperature T_p, which can then be converted into an electron density n_e with the knowledge of the loop width w. The so-obtained electron densities are shown for loop 3 as a function of the loop position

s/L in Figure 7 (*middle*). Since the loop density $n_e(s[h])$ is generally a function of the height, we fit a hydrostatic model that has a density (or pressure) scale height λ_T constrained by the average loop temperature $T_e = T_p$,

$$\lambda_T(T_e) = \frac{2k_B T_e}{\mu m_H \, g_\odot} \approx 47 \left(\frac{T_e}{1 \, \text{MK}} \right) \, \text{Mm}, \qquad (10)$$

where $\mu \approx 1.27$ is the mean molecular weight for the solar corona (with a hydrogen-to-helium ratio of H : He = 10 : 1), m_H is the mass of the hydrogen atom, $g_\odot$ the solar gravity, and k_B the

Boltzmann constant. Neglecting the variation of solar gravity with height, the density (or pressure) is expected to follow an exponential height dependence in hydrostatic equilibrium,

$$n_e(h) = n_0 \exp\left(-\frac{h}{\lambda_T}\right), \qquad (11)$$

where n_0 represents the base density. This base density is found to be $n_0^A = 1.8 \times 10^9$ cm^{-3} for loop 3 using the *STEREO A* images (Fig. 7, *middle left*), and $n_0^B = 1.7 \times 10^9$ cm^{-3} using the *STEREO B* images (Fig. 7, *middle right*). The scale height for loop 3 is $\lambda_T = 54$ Mm based on the mean temperature of $T_p = 1.16$ MK for the set of *STEREO A* images. We also measure the mean deviation of the measured densities $n_e(s[h])$ along the loop from the hydrostatic model $n_e^{\mathrm{model}}(h)$ (eq. [11]) and find deviations of $n_e/n_e^{\mathrm{model}} = 1.00 \pm 0.25$ for loop 3 with *STEREO A*, so the observations agree with the hydrostatic model within $\approx 25\%$ in both *STEREO A* and *B*.

A display of the density profiles $n_e(s)$ of all 30 loops is shown in Figure 10, along with the fits of the hydrostatic models. The deviations of most density measurements from the hydrostatic model are on the order of $\approx 37\% \pm 9\%$ (see Table 3, col. [10]; i.e., standard deviation of n_e/n_e^{model}). Since the height range ($h \approx 10$–30 Mm) of most loops is less than a thermal scale height ($\lambda_T \approx 45$–65 Mm), the height dependence of the hydrostatic model is not very pronounced in the fitted loop segments, but the loop densities clearly follow the hydrostatic trend in a number of cases (e.g., loops 3, 4, 8, 13, 14, and 27). Statistically, we find an average base density of $n_0 = (1.4 \pm 0.3) \times 10^9$ cm^{-3}. However, if we correct for the unresolved loop widths (eq. [8]), we obtain an average base density that is a factor of 1.6 higher, namely, $n_c = (2.2 \pm 0.5) \times 10^9$ cm^{-3}. The resolution-corrected density values are given in Table 3 (in parentheses of col. [9]), using the corrected loop widths also given in Table 3 (in parentheses of col. [4]). The consistency of average density values is $n_A/n_B = 0.94 \pm 0.12$ between the two *STEREO A* and *B* spacecraft (Fig. 8, *middle left*). This average density of loops observed in 171 Å is fully consistent with other loop samples measured in the same wavelength, e.g., $n_e = (1.92 \pm 0.56) \times 10^9$ cm^{-3} with EIT (Aschwanden et al. 2000a) or $n_e \approx (2.0 \pm 0.5) \times 10^9$ cm^{-3} with *TRACE* (Aschwanden et al. 2000b).

3.5. *Loop Widths*

We measured the loop width w by the equivalent width of the background-subtracted cross-sectional flux profiles at n_s loop positions in all three filters for both the *STEREO A* and *B* spacecraft. We expect that the loop widths are bound at the lower end by the width of the point-spread function, and at the upper end by the inner width of the background zone, which is 4 EUVI pixels (≈ 4.6 Mm). We show in Figure 11 (*bottom panel*) the distribution of average loop widths measured in both the *STEREO A* and *B* spacecraft in the filter that has the highest sensitivity for the loop DEM peak temperature T_p, which is mostly either the 171 or 195 Å filter. The mean and standard deviation of these 60 measurements is $w = 2.68 \pm 0.18$ Mm, which is close to the instrumental resolution of EUVI. If we interpret the lower cutoff of the width distribution in terms of the instrumental resolution, we obtain a value of $w_{\min} = 2.84$ Mm ($= 3.4'' = 2.15$ EUVI pixels), which is close to the preliminary determination of the spatial resolution of EUVI *B* from the lunar transit ($w_{\mathrm{res}} = 2.5$ Mm $= 3.6'' = 2.25$ EUVI pixels; Lemen et al. 2007). We therefore conclude that all the analyzed features are unresolved loops with true widths that are smaller than the EUVI resolution. The fact that we

measure some widths below the instrumental resolution reflects uncertainties caused by inaccurate background subtractions. Anyway, if we assume that the true loop width w_c and the width of the point-spread function add in quadrature, we can estimate the true width of loops with $w > w_{\mathrm{res}}$ from equation (7), from which we obtain a distribution with a mean and standard deviation of $w_c = 1.12 \pm 0.35$ Mm (Fig. 11, *bottom panel*).

It is interesting to compare the results from EUVI with *TRACE*, which has a spatial resolution that is about 3 times better, namely, $2.5 \times 0.5'' \times 0.725$ Mm $= 0.91$ Mm (Golub et al. 1999). A sample of 2512 loop widths measured from cospatial Gaussian plus linear background triple-filter fits yielded a distribution of $w = 1.42 \pm 0.34$ Mm (Aschwanden & Nightingale 2005), which after correction for the point-spread function yields an estimated true width of $w_c = 1.13 \pm 0.40$ Mm, similar to the corrected widths from EUVI. In fact, if we use the corrected loop widths from the *TRACE* sample to predict the observed widths with EUVI, by adding the point-spread function in quadrature, i.e., $w = (w_c^2 + w_{\mathrm{res}}^2)^{1/2}$, we predict a distribution with a mean and standard deviation of $w = 2.71 \pm 0.16$ Mm (Fig. 11, *middle panel*), which closely coincides with the observed distribution $w = 2.68 \pm 0.18$ Mm. Thus, the loop widths obtained from EUVI observations are consistent with those from *TRACE* after correction for the instrumental point-spread function. This has the far-reaching consequence that the unresolved loops seen with EUVI appear to correspond to the same elementary loop strands that are resolved with *TRACE* and thus are expected to be near isothermal (according to the triple-filter analysis of Aschwanden & Nightingale 2005). This conclusion is consistent with our finding of near-isothermal loop temperatures within a relatively small variation of $\sigma_T/T_p \lesssim 0.2$. However, we have to add a caveat that we cannot exclude a scenario of unresolved loop strands with a narrow temperature distribution and some filling factor below unity. But since EUVI has a poorer angular resolution than *TRACE*, it also produces more contamination in the background subtraction and thus is not the most suitable instrument for discriminating isothermal from multithermal DEMs.

3.6. *Diagnostic of Loop Cooling*

Stereoscopy provides us for the first time with a method for measuring the loop length precisely, since the 3D coordinates (x_i, y_i, z_i) are required to calculate the full length in 3D space,

$$2L = \sum_{i=2}^{n_s} \sqrt{(x_i - x_{i-1})^2 + (y_i - y_{i-1})^2 + (z_i - z_{i-1})^2}. \quad (12)$$

The combination of the loop half-length L, the loop maximum temperature $T_{\max}$, and the base density n_0 yield all three ingredients to test coronal loop scaling laws. As a first test we apply our measurements to the RTV (Rosner et al. 1978) law, which assumes a constant pressure p_{RTV} and a uniform heating function throughout the loop,

$$p_{\mathrm{RTV}} = \frac{1}{L}\left(\frac{T_{\max}}{1400}\right)^3, \qquad (13)$$

while the observed loop pressure p_{obs} can be calculated from the ideal gas law, using the measurements of the base density $n_e = n_0$ and loop apex temperature $T_{\max} \approx T_p$,

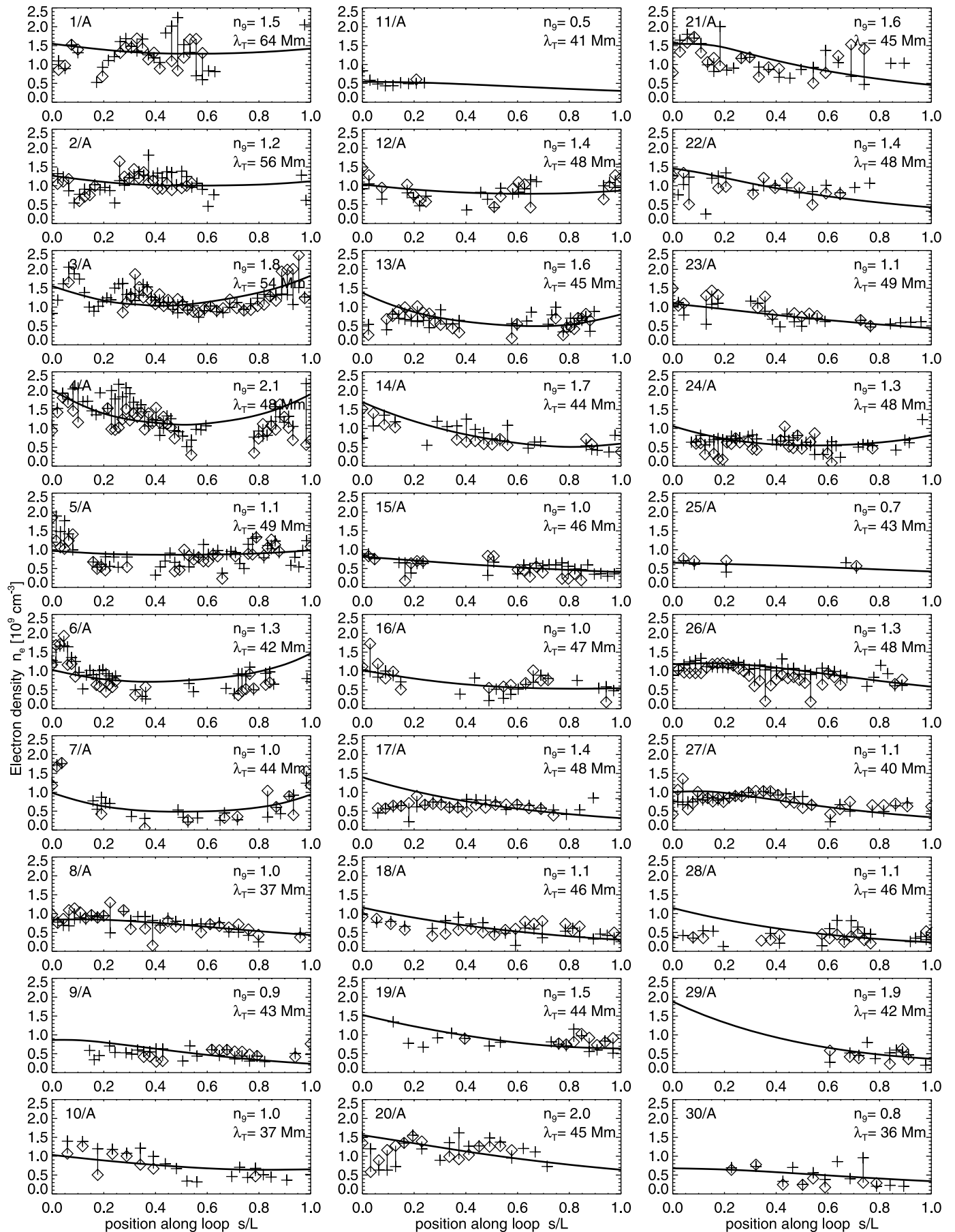$$p_{\mathrm{obs}} = 2n_0 k_{\mathrm{B}} T_p. \qquad (14)$$

FIG. 10.—Density profiles measured for all 30 loops with *STEREO A* (*crosses*) and *STEREO B* (*diamonds*). A one-parameter hydrostatic model is fitted for the base density n_0 (of *STEREO A*), using the thermal scale height λ_T predicted by the mean loop temperature (*thick curve*). The loop number is indicated in the top left corner of each frame; the base density (in units of $n_9 = n_0/10^9$ cm^{-3}) and the thermal scale height λ_T (in units of Mm) are indicated in the top right corners of each frame. Note that only loops 1–7 are complete loops (including two footpoints), while all others are incomplete loop segments, mostly ending below the loop apex (showing a monotonically decreasing density function).
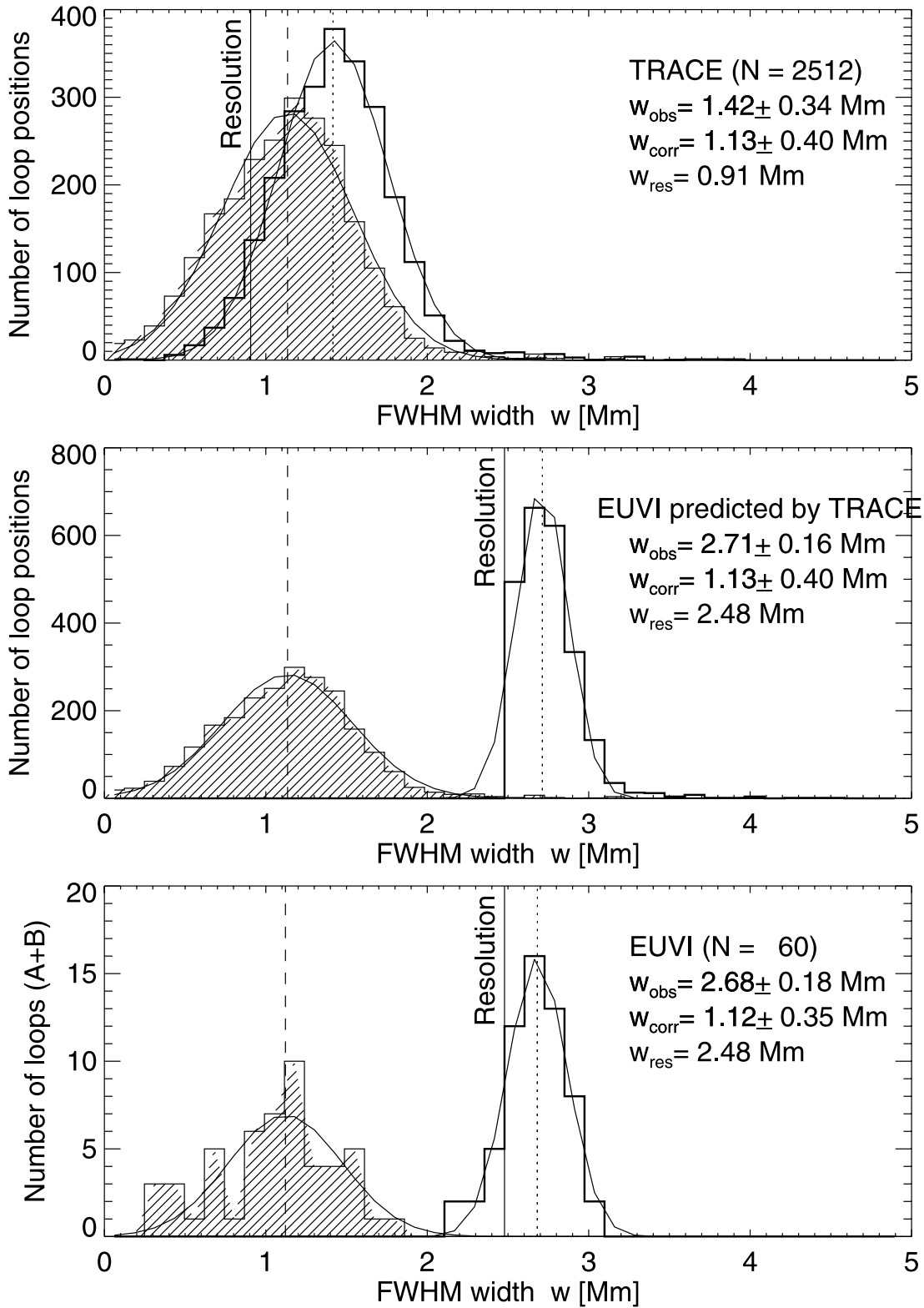
Fig. 11.—Distribution of 1073 loop width measurements in 30 loops observed with *STEREO* EUVI *A* and *B* (*bottom panel*), uncorrected (*white histogram*), as well as corrected for the spatial resolution of 2.15 EUVI pixels (*hatched histogram*). A distribution of 2512 loop widths measured with *TRACE* (Aschwanden & Nightingale 2005) is also shown for comparison (*top panel*), as well as the predicted distribution of loop widths as they would be measured by an instrument with the resolution of EUVI (*middle panel*). Note that *TRACE* has about a three times better spatial resolution, but the resolution-corrected distributions of EUVI and *TRACE* loop widths are very similar, and thus the predicted distribution also matches the observed one closely.
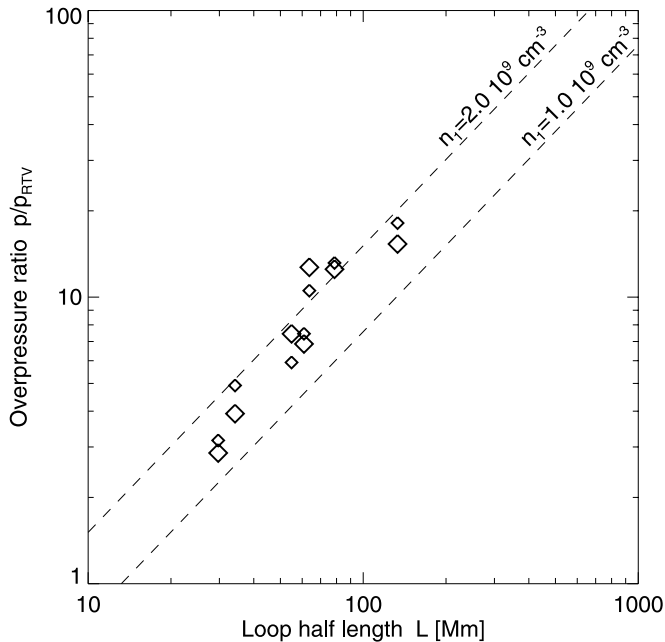
Fig. 12.—Loop overpressure factor $q_p = p/p_{RTV}$ (normalized by Rosner-Tucker-Vaiana scaling law with uniform heating) vs. loop half-length L. Data points are given for the seven complete loops detected along their full length, measured with *STEREO A* (*large diamonds*) and with *STEREO B* (*small diamonds*).

The ratio of the observed loop pressure p_{obs} to the pressure p_{RTV} predicted by the RTV law is also called the overpressure (or overdensity) ratio,

$$ q = \frac{n_{obs}}{n_{RTV}} = \frac{p_{obs}}{p_{RTV}} = \frac{2n_0 k_B T_e}{(1/L)(T_e/1400)^3} = \frac{c_0 n_0 L}{T_e^2}, \quad (15) $$

with the constant $c_0 = 2k_B 1400^3 = 7.57 \times 10^{-7}$ (in cgs units). For coronal loops in RTV energy balance this ratio should be near unity, or within a factor of $\lesssim 2$ for footpoint (nonuniform) heating (Serio et al. 1981; Aschwanden & Schrijver 2002; Winebarger et al. 2003). We plot the overpressure ratio q of the seven loops with known loop lengths in Figure 12 as a function of the loop length L and find that the loops exhibit an overpressure in the range of ≈ 3–20, a result that is similar to earlier findings from *TRACE* (Lenz et al. 1999; Aschwanden et al. 2000b) and EIT (Aschwanden et al. 2000a) and cannot be explained by equilibrium models (with balanced heating and cooling rates).

Overpressures are known to arise in the nonequilibrium state of the cooling phase of impulsively heated loops, as they were simulated with numerical hydrodynamic codes (e.g., Jakimiec et al. 1992; Warren et al. 2002; Cargill & Klimchuk 2004) and observed in loops subsequently in soft X-rays and EUV (Warren et al. 2002; Winebarger & Warren 2005). While the loops exhibit an underpressure during the heating phase, they develop a gradually increasing overpressure during the cooling phase. The preceding heating phase should be readily detectable in soft X-rays, e.g., with *Hinode* XRT.

4. DISCUSSION

4.1. *Comments on Background Definitions in Previous Loop Modeling*

If we were only interested in statistical temperature distributions of the solar corona, we would not need any background subtraction and could just model the EUV or soft X-ray total flux measured in various temperature filters by forward fitting of a parameterized DEM distribution function convolved with the filter response functions. Such full-corona DEMs have been inferred in a number of studies, for instance with EIT data (e.g., Zhang et al. 1999) or with *Yohkoh* SXT data (e.g., Aschwanden & Acton 2001).

However, if we are interested in determining the temperature and density of coronal loops, we have first to define a loop structure and then subtract the loop-unrelated flux (in the foreground and background of the loop) along a given line of sight. While the location of a loop, defined by a curved flux tube following a particular magnetic field line from one footpoint to the other, can often be identified in an image, the definition of the loop cross section is more difficult and strongly depends on the spatial resolution of the instrument. It has clearly been demonstrated that loops seen with low spatial resolution turn out to be composed of fine strands that can only be resolved with instruments of higher resolution. The question arises whether the substructuring of loop strands continues to infinity, which makes the definition of a loop cross section and thus the loop background definition highly ambiguous. Fortunately, a discovery of fundamental importance has recently been made regarding the loop substructuring, using the *TRACE* instrument, which currently owns the highest spatial resolution in EUV imaging. From triple-filter modeling it was found that loop strands with a cross-sectional width of $w_{obs} = 1.42 \pm 0.34$ Mm (Fig. 11, *top*) have a near-isothermal temperature cross section, while virtually all loops with larger widths are multithermal and therefore are of composite nature. This significant finding defines an *elementary loop strand* with the properties of a cross section with homogeneous density and temperature that can be modeled with 1D hydrodynamic models. The extraction of such elementary loops requires a background subtraction that filters out all structures with widths of $\gtrsim 2$ Mm (or $\gtrsim 3''$). Only the *TRACE* instrument has sufficient spatial resolution ($\approx 1''$) to properly model the background around such fine strands, while other instruments (*SOHO* EIT, CDS, and *Yohkoh*) do not resolve these finest loop strands and thus cannot establish a suitable background model with sufficient accuracy. Even with EUVI, which has a resolution of $\approx 3.4''$, we observe that the finest loop widths appear to be near the instrumental resolution, but correcting for the point-spread function we find a similar width distribution to that with *TRACE* (Fig. 11, *bottom*). So, the overriding requirement of a suitable background subtraction is to model the background level close to the edge of an elementary loop, while all attempts to establish a background far away from the loop axis are unsuitable and yield gross underestimates. Essentially, the farther away the background is evaluated, the lower is the background flux, which can be used as a criterion for the expected background contamination. In this study we found that the loop flux amounts only to $11\% \pm 4\%$ of the total flux, consistent with measurements from *TRACE*, where a flux-to-background contrast of $18\% \pm 13\%$ was found for elementary loops (Aschwanden & Nightingale 2005; Aschwanden 2005).

In some previous studies, no background was subtracted at all in the temperature analysis of a loop (Schmelz et al. 2001; Schmelz 2002), or the background has been arbitrarily chosen from a dark image section far away from the loop axis (e.g., Priest et al. 2000). Reale (2002) estimates that the background subtraction (including only the scattered light) by Priest et al. (2000) amounts only to $\lesssim 20\%$ and chooses a higher background level of $\approx 50\%$, but we suspect that this level is still substantially too low. The same loop was modeled with a two-component temperature model, and a background of $\approx 80\%$ was found to be more suitable for

extracting the high-temperature loop (Aschwanden 2001). In other studies (Schmelz et al. 2003, 2005, 2007; Schmelz & Martens 2006), an attempt at background subtraction is made by choosing dark pixels about $20''$ (≈ 14 Mm) away from the traced loop axis, and the authors sometimes find a narrower temperature range for the loop than without background subtraction but often still find a broad temperature range due to the overwhelming contamination by the unsubtracted-background corona. Studies that evaluate the background close to the loop edges generally find near-isothermal loops. The proximity of the location of the evaluated background to the loop axis is reflected in the measured loop width, i.e., $w \approx 7$ Mm for loops analyzed from EIT (Aschwanden et al. 1999; 2000a), $w \approx 4$ Mm for a loop analyzed from *TRACE* and *SOHO* CDS (Del Zanna & Mason 2003), or $w \approx 1.4$ Mm for loops analyzed from *TRACE* (Aschwanden & Nightingale 2005).

In summary, the main criteria for extracting elementary loops from the background corona are (1) a loop widths of $w \lesssim 2.0$ Mm and (2) a flux-to-background contrast of $f_{\text{loop}}/f_{\text{back}} \lesssim 0.1$. Any loop feature extracted with larger widths or lower background levels is likely to be composed of multiple (multitemperature) loop strands or to be heavily contaminated by the background corona.

4.2. *What Is New about Density and Temperature Diagnostics with STEREO?*

This is the first study in which we employ dual spacecraft data from the *STEREO* mission. The reader or future data user may wonder what is new about the *STEREO* mission regarding density and temperature diagnostics of coronal loops. *STEREO* EUVI has the same choice of wavelength filters in 171, 195, and 284 Å as *SOHO* EIT and *TRACE*, but an intermediate spatial resolution: $1.2''$ for *TRACE*, $\approx 3.4''$ for EUVI, and $\approx 6''$ for *SOHO* EIT. However, the trade-off of a lower spatial resolution than *TRACE* is compensated with a full-Sun field of view, while *TRACE* has only an $8'$ field of view. Therefore, the density and temperature diagnostics seems to be the same, with three coronal filters in identical wavelengths, but the lower spatial resolution than *TRACE* actually also affects the accuracy of the density and temperature determination due to background uncertainties.

What is really new is the dual (stereoscopic) viewing angle, which not only allows us a full 3D reconstruction of individual loops, but also provides an unprecedented consistency check between two different background subtractions from two different viewing angles, which increases the accuracy in the determination of loop-associated physical parameters, such as the electron density, temperature, and width. The dual background modeling from two different viewing angles yields a realistic estimate of the uncertainties of (background-subtracted) loop quantities and can even be used to bootstrap the background modeling at the less favorable viewing angle (not attempted here). The two independent background evaluations are very important because the accuracy of the background modeling definition is the main limitation of the accuracy of measured loop densities and temperatures.

Another bonus of the stereoscopically determined 3D geometry of coronal loops is the knowledge of the loop inclination angle, yielding the vertical density (or pressure) scale height $\lambda_p = \lambda_{\text{obs}} \cos \vartheta$, which is the relevant parameter required for modeling of the hydrodynamic momentum balance. Another parameter that can only be determined properly with 3D coordinates is the absolute loop length L, which had to be estimated from the projected length and guesstimated viewing angle between the line of sight and the loop plane in previous single-spacecraft images. The knowledge of the loop length L is a prerequisite for any test of loop scaling laws. The RTV law requires the measurement of

the loop length L, loop maximum temperature $T_{\max}$, and loop pressure p_0 (or density n_0), which can all be properly measured with *STEREO* EUVI. Therefore, for the first time we can perform accurate tests of loop scaling laws.

There is a host of new tasks that can be accomplished with *STEREO* that have not been tackled before. The measurement of the 3D coordinates of a loop can be extended in time, providing us with accurate position, velocity, and acceleration parameters of loop motions, loop expansions, or loop shrinkage, which can be modeled in the context of hydrodynamics and reconnection theory. The 3D geometry should also allow us to measure the twist angle of a loop or the change in the twist angle, which yields crucial information on the nonpotentiality of the magnetic field and current loading in loop systems. Furthermore, the 3D geometry of individual loops can be used as a skeleton for a full 3D reconstruction of the plasma in an active region, by multiscale tracing of loop structures and directional interpolation. Such full 3D renderings of active region plasmas aid the determination of the spatial heating function with statistical methods (e.g., see full-Sun visualizations by Schrijver et al. 2004).

5. CONCLUSIONS

In this study we performed the first density and temperature diagnostics of coronal loops with the *STEREO* EUVI spacecraft *A*(head) and *B*(ehind). As a disclaimer we should be aware that the analysis presented here is based on preliminary determinations of the EUVI temperature response functions (Fig. 2) and EUVI spatial resolution. We modeled the density $n_e(s)$ and temperature $T_p(s)$ at the peak of the differential emission measure (DEM) distribution as a function of the loop length s for a set 30 loops, for which we determined the 3D geometry in Paper I. Our results and conclusions can be summarized as follows:

1. The determination of loop densities and temperatures is very sensitive to the *background definition*, which has to be modeled very close to the loop edges. We found that a cubic polynomial interpolation of the background on both sides of a loop yields the most reliable technique. With proper background subtraction we find that the loop-associated flux amounts only to about 10% of the total flux for the finest loop structures. Since this result is also consistent with *TRACE* studies with higher spatial resolution, we conclude that all previous studies that subtracted out significantly less than 90% background must consist of multiple loop strands or contain heavy contaminations from the background corona.

2. The *self-consistency between the two STEREO spacecraft* was found to be accurate within a few percent regarding the measurement of loop fluxes, densities, temperatures, and widths. Differences in the measurements between the two spacecraft are mostly dominated by uncertainties in the definition of two different backgrounds from two different viewing angles, rather than calibration uncertainties.

3. *Electron temperatures* of loops were found in the entire sensitivity range of the 171 Å filter, in which the loops were originally detected, from the coolest loop with $T_p = 0.9 \pm 0.2$ MK to a hottest loop with $T_p = 1.4 \pm 0.4$ MK. The random fluctuations of temperatures $T_p(s)$ along the loops due to background subtraction uncertainties were found to be larger ($\sigma_T/T_p \approx 0.25$) than any systematic temperature variation along the loops. Thus, we find near-isothermal loops within this limit. This could mean that we observe either elementary isothermal loop strands or a possible superposition of multiple, cooling threads with a narrow DEM (see, e.g., Warren et al. 2002).

4. *Electron densities* were measured in the range of $n_e = (2.2 \pm 0.5) \times 10^9$ cm^{-3}, after correction for the point-spread function,

which are fully consistent with other samples of loops detected in the same wavelength filter, such as with EIT (Aschwanden et al. 2000a) or *TRACE* (Aschwanden et al. 2000b). While most of the loops fade out at a height of about 1 density scale height, some clearly show a density variation versus height according to the hydrostatic gravitational stratification.

5. *Loop widths* have been measured with a mean and standard deviation of $w = 2.6 \pm 0.1$ Mm, which coincides with the EUVI spatial resolution. The selected loops (using a high-pass filter in Paper I) are therefore all unresolved loop strands. Correcting for the point-spread function we estimate their true widths to be $w_c = 1.1 \pm 0.3$ Mm, which is similar to elementary loop strands resolved with *TRACE*, which have a corrected width of $w_c = 1.1 \pm 0.4$ Mm. The analyzed loops could therefore be consistent with elementary loops with isothermal cross sections as seen with *TRACE*, but we cannot exclude a multithread scenario given the spatial resolution of EUVI.

6. The measurement of the true loop length allows us for the first time an accurate test of *loop scaling laws*. We find that none of the loops is consistent with the RTV law, while they exhibit an overpressure by factors of ≈ 3–20 and are more consistent with the nonequilibrium cooling phase of loops previously heated to higher temperatures, similar to earlier studies with SXT, EIT, and *TRACE*.

Thus, we have demonstrated a suitable technique of density and temperature diagnostics with the *STEREO* EUVI spacecraft. On the one hand, we found fairly consistent results compared with earlier *TRACE* or EIT studies, although we deal with a different spatial resolution, while on the other hand, we find that the accuracy of density diagnostics crucially depends on the background subtraction technique, a point that was often ignored in earlier studies but can be systematically investigated using double checks from the two stereoscopic spacecraft. In future studies we will focus on the time evolution, hydrodynamic modeling, and magnetic modeling of stereoscopically reconstructed coronal loops, as well as on 3D plasma rendering of entire active regions.

REFERENCES

Aschwanden, M. J. 2001, ApJ, 559, L171
———. 2005, ApJ, 634, L193
Aschwanden, M. J., & Acton, L. W. 2001, ApJ, 550, 475
Aschwanden, M. J., Alexander, D., Hurlburt, N., Newmark, J. S., Neupert, W. M., Klimchuk, J. A., & Gary, G. A. 2000a, ApJ, 531, 1129
Aschwanden, M. J., Newmark, J. S., Delaboudinière, J.-P., Neupert, W. M., Klimchuk, J. A., Gary, G. A., Portier-Fornazzi, F., & Zucker, A. 1999, ApJ, 515, 842
Aschwanden, M. J., & Nightingale, R. W. 2005, ApJ, 633, 499
Aschwanden, M. J., Nightingale, R. W., & Alexander, D. 2000b, ApJ, 541, 1059
Aschwanden, M. J., & Schrijver, C. J. 2002, ApJS, 142, 269
Aschwanden, M. J., Wuelser, J. P., Nitta, N. V., & Lemen, J. R. 2008, ApJ, 679, 827 (Paper I)
Cargill, P. J., & Klimchuk, J. A. 2004, ApJ, 605, 911
Del Zanna, G., & Mason, H. E. 2003, A&A, 406, 1089
Feldman, U. 1992, Phys. Scr., 46, 202
Golub, L., et al. 1999, Phys. Plasmas, 6, 2205
Jakimiec, J., Sylwester, B., Sylwester, J., Serio, S., Peres, G., & Reale, F. 1992, A&A, 253, 269
Klimchuk, J. A., Patsourakos, S., & Cargill, P. J. 2008, ApJ, in press
Lemen, J. R., Wuelser, J. P., Nitta, N. V., & Aschwanden, M. J. 2007, BAAS, 210, 28.01
Lenz, D. D., DeLuca, E. E., Golub, L., Rosner, R., & Bookbinder, J. A. 1999, ApJ, 517, L155
Mazzotta, P., Mazzitelli, G., Colafrancesco, S., & Vittorio, N. 1998, A&AS, 133, 403

Priest, E. R., Foley, C. R., Heyvaerts, J., Arber, T. D., Mackay, D., Culhane, J. L., & Acton, L. W. 2000, ApJ, 539, 1002
Reale, F. 2002, ApJ, 580, 566
Rosner, R., Tucker, W. H., & Vaiana, G. S. 1978, ApJ, 220, 643
Schmelz, J. T. 2002, ApJ, 578, L161
Schmelz, J. T., Beene, J. E., Nasraoui, K., Blevins, H. T., Martens, P. C. H., & Cirtain, J. W. 2003, ApJ, 599, 604
Schmelz, J. T., & Martens, P. C. H. 2006, ApJ, 636, L49
Schmelz, J. T., Nasraoui, K., Del Zanna, G., Cirtain, J. W., DeLuca, E. E., & Mason, H. E. 2007, ApJ, 658, L119
Schmelz, J. T., Nasraoui, K., Richardson, V. L., Hubbard, P. J., Nevels, C. R., & Beene, J. E. 2005, ApJ, 627, L81
Schmelz, J. T., Scopes, R. T., Cirtain, J. W., Winter, H. D., & Allen, J. D. 2001, ApJ, 556, 896
Schrijver, C. J., Sandman, A. W., Aschwanden, M. J., & DeRosa, M. L. 2004, ApJ, 615, 512
Serio, S., Peres, G., Vaiana, G. S., Golub, L., & Rosner, R. 1981, ApJ, 243, 288
Warren, H. P., Winebarger, A. R., & Hamlton, P. S. 2002, ApJ, 579, L41
Winebarger, A. R., & Warren, H. P. 2005, ApJ, 626, 543
Winebarger, A. R., Warren, H. P., & Mariska, J. T. 2003, ApJ, 587, 439
Wuelser, J. P., et al. 2004, Proc. SPIE, 5171, 111
Young, P. R., Del Zanna, G., Landi, E., Dere, K. P., Mason, H. E., & Landini, M. 2003, ApJS, 144, 135
Zhang, J., White, S. M., & Kundu, M. R. 1999, ApJ, 527, 977